Design and Development of High-Power Pulse Transmitters for Underground Environmental Perception

by

Adil Karimov

A thesis submitted in partial fulfillment of the requirements for the degree of

Master of Science

in

Electromagnetics and Microwaves

Department of Electrical and Computer Engineering
University of Alberta

Abstract

The objective of this thesis is associated with designing a high-power Gaussian pulse transmitter for high-depth imaging applications. Two types of pulse transmitters are presented in this work. The former configuration is based on Step Recovery Diodes (SRDs), while the latter is based on Nonlinear Transmission Lines (NLTLs). Both configurations are thoroughly studied and tested theoretically and experimentally.

The first system consists of three main parts: an avalanche transistor-based pulse shaping network, an improved *SRD*-based configuration, and a pulse-shifting circuit with a broadband combiner to create a second derivative Gaussian pulse for high-power applications. A Gaussian pulse transmitter comprises a Gaussian pulse shaping network that converts a sine/square signal to a first derivative Gaussian pulse, the monopulse. The monopulse is used to excite the antenna to radiate through the medium. The pulse width and amplitude of a monopulse determine the image resolution and detection range, respectively. The transistor-based circuit plays a role as an input pulse generator for the *SRD* pulse shaping circuit that produces ultra-short pulses. The *SRD*-based part of the circuit is developed to have a high amplitude output pulse. A balun is accommodated at the output of the avalanche circuit to convert the output pulse into two opposite polarity pulses. Two parallel *SRD*-based pulse shaping networks are placed after the balun to sharpen the output pulses of the avalanche circuit. The outputs of these two branches are two oppositely polarized narrow Gaussian pulses. Note that a delay line is attached for one of the branches to provide the delay between the two opposite pulses. A broadband combiner is used after the two *SRD*-based circuits to add the opposite pulses. The final output of the combiner is a monopulse. The last part of the transmitter can be any broadband antenna such as a Vivaldi antenna or a monopole antenna placed after the combiner to radiate the monopulse.

In order to check the validity of the transmitter for imaging purposes, several experiments for buried objects in the sand are conducted. All reconstructed 3D images clearly represent the target shape and dimension, confirming the practicality (functionality) of the designed transmitter for sensing and imaging applications.

The second configuration is the Gaussian pulse generator based on the NLTL. The NLTL consists of the twenty-one cascaded unit cells of transmission lines with reversed biased varactors connected in parallel, which sharpen the rising edge. An analysis of the sharpening process of the rising and falling time of a Gaussian pulse is presented in this thesis. Several different simulations and circuit tests were established to conduct the analysis, including a lumped-element model and a distributed-element model.

Preface

This thesis is an original work by Adil Karimov. The technical apparatus referred to in chapters I-III was designed by myself, with the assistance of Rouhollah Feghhi. The data analysis and concluding experiments in chapter IV are my original work and the literature review.

Chapter I-III of this thesis has been published as Adil Karimov, Rouhollah Feghhi, Fatemeh Modares Sabzevari, Robert S. C. Winter, Robert Fedosejevs, and Karumudi Rambabu, "Design and Development of a High-Power Pulse Transmitter for Underground Environmental Perception," IEEE Transactions on Microwave Theory and Techniques. I was responsible for the data collection and analysis and the manuscript composition. Rouhollah Feghhi assisted with the data collection and contributed to manuscript edits. Fatemeh Modares Sabzevari and Robert S. C. Winter helped with the application sections by conducting imaging experiments for the system validation.

Acknowledgements

First and foremost, I would like to thank my supervisor, Dr. Rambabu Karumudi and co-supervisor, Dr. Robert Fedosejevs, for giving me the opportunity to come and study at one of the top universities in Canada, the University of Alberta. Even though it was difficult initially, I could broaden my horizons and succeed in the MSc program with their trust, mentorship, and guidance.

Also, I am grateful to Rouhollah Feghhi for helping throughout my study. Mr. Feghhi helped me a lot in understanding the basics of transmission lines and circuit design. With Mr. Feghhi's mentorship, I obtained new practical and theoretical skills. Moreover, I am glad to have friendly colleagues, Kapil Gangwar, Mahdi Alesheikh, Fatemeh Modares and Robert Winter, for their collaboration. Ms. Modares and Mr. Winter helped me a lot with the experimental setups for imaging applications.

The author would like to thank the Bolashak International Scholarship programme for providing a scholarship to support my study. The author would like to thank the Institute for Oil Sands Innovation (IOSI) at the University of Alberta and the Natural Sciences and Engineering Research Council of Canada (NSERC) for their support and funding.

Contents

List of Tables

List of Figures

Chapter I

Introduction

Advantages of Ultra-wideband (UWB) radar technology over conventional ground penetrating radar (GPR) are having much-developed system precision in detecting various objects, including metal and non-metal objects. Underground environmental perception radar can provide non-contact and real-time details of the buried objects, such as their location, shape, and dimensions.

Ultra-wideband (UWB) radars are devices involving the generation and transmission of very short radio-frequency (RF) pulses, typically in the sub-nanosecond range, that span a very large frequency range.

According to the Canadian Radio Standards Specification RSS-220, a UWB device is a type of radiator with either a -10 dB bandwidth of 500 MHz and more or a -10 dB fractional bandwidth greater than 0.2. Moreover, the -10 dB bandwidth for radar imaging devices shall be entirely below 10.6 GHz [1].

The fractional bandwidth is defined as follows.

$$\mu_{-10} = \frac{B_{-10}}{f_C} = 2\left(\frac{f_H - f_L}{f_H + f_L}\right) \tag{1}$$

Where, f_H is the highest frequency at which the power spectral density of the UWB transmission is -10 dB of its peak value; f_L is the lowest frequency at which the power spectral density of the UWB transmission is -10 dB of its peak value, and f_C is the center frequency of the -10 dB bandwidth.

UWB pulses have good spatial resolution, enabling penetration in dielectric materials, and can be used for sensing and imaging applications. Radar imaging systems can obtain images of obstructed and hidden objects. This work will present the design and development of high-power pulse transmitters for underground environmental perception and penetration of other lossy dielectric material. The energy from the radar is intentionally directed down into the ground for this purpose. For the present studies, the system will be used only in an indoor environment. Hence, the FCC regulations for outdoor applications are not applicable.

The main requirements for the environmental underground perception radar are to have enough power for penetrating into the ground and also to have a narrow enough pulse width to obtain high resolution detection.

The resolution detection or range resolution is a criterion where the peaks of the overlapped reflected pulses should be separated by at least half of their peak values. In other words, the range resolution is a minimum distance between objects (or parts of an object) where radar can detect them as separate parts. The radar range resolution for a square wave in frequency space is defined as follows [2].

$$\Delta_R = \frac{c}{2(BW)\sqrt{\varepsilon_{medium}}} \tag{2}$$

Where c is the speed of light in vacuum and $c/\sqrt{\varepsilon_{medium}}$ is the speed of propagation of light in the medium. In our case, sand is used as a medium which has a permittivity of$\varepsilon_{sand} = 2.6$, and BW is the zero-crossing bandwidth of the pulse. Our system aims to have a 3 GHz bandwidth. Thus, the radar range resolution is approximately 0.03 m.

Furthermore, the range resolution in terms of pulse width can be written as [3].

$$\Delta_R = \frac{c\tau}{2\sqrt{\varepsilon_{medium}}} \tag{3}$$

Where c/$\sqrt{\varepsilon_{medium}}$ is a speed of light in the medium, and τ is the pulse width of the radiated pulse.

Hence, by using the above formula, one can find the range resolution for a transmitting pulse of 200 ps is 0.0186 m. If the distance between two detecting objects is less than 0.018 m, the radar will detect the objects as one object.

The peak power required for detecting an object depends on the medium attenuation, target radar cross-section, antenna gain, operating frequency bandwidth and distance to the object. For example, the minimum peak power required for detecting a 10 x 10 cm^2 metal object is 4.7 W if the object is buried in dry sand at a 2.3 m depth [4]. The goal of this project was to develop techniques to generate a pulses of peak power of 5 W and a pulse width of no more than 200 ps for such imaging applications.

1.1 Application

One potential application of the proposed system is the construction industry, where environmental sensors play a critical role in autonomously operated robotic systems. UWB radars based on diodes can produce Gaussian pulses suitable for object detection. A variety of applications range from sensing to imaging, such as characterization of objects buried in the ground, pavement damage detection, localization, and imaging of objects [5]-[8]. Recently UWB sensors have been used for multiphase flow metering [9], human vital sign measurements [10], people tracking [11], medical imaging [12], and underground scanning and imaging [13]. A higher range resolution is required to obtain high accuracy sensing and requires a narrower pulse width [14]. A high-power Gaussian pulse can improve the radar detection range [15]. It is challenging to design a *UWB* pulse source with high pulse amplitude and narrow pulse width in the range of a couple of hundred picoseconds. Such high-quality pulses are required in some applications, such as oil well perforation monitoring [16], [17], and microwave breast imaging in biomedical applications [18]-[20].

1.2 Literature review

The literature presents various ways of generating Gaussian pulses, such as the systems that implement tunnelling diodes (*TD*), and bipolar junction transistors (*BJT*), which operate in avalanche regions. Also, *CMOS* technology, step recovery diodes (*SRD*), and nonlinear transmission lines (*NLTL*) [21] have gained a lot of attention thanks to low cost and ease of fabrication. Moreover, the *TD*s produce low amplitude pulses with a fast rise time, in the order of tens of picoseconds [22]. Avalanche transistors are suitable for producing high voltage pulses with a pulse width of a few nanoseconds. The avalanche transistors typically work with low pulse repetition frequency in the range of a few kilohertz, [23]-[26]. Using CMOS technology, integrated circuit pulse generators provide a narrow pulse width with a limited pulse amplitude. However, *SRD*-based pulse generators are appropriate for generating an optimal pulse width and amplitude. Nevertheless, these methods cannot satisfy both high amplitude and narrow pulse width for high detection range and image resolution.

NLTLs have complex configurations which can significantly sharpen the rise/fall time of the input pulse and produce a narrower pulse width at the output [27]-[29]. Many authors have mentioned the valuable characteristic of the NLTLs [30]-[49]. Hirota and Suzuki, back in the 70s, observed the fundamental properties of solitons generated by the nonlinear LC network [28]. Rodwell *et al.* explicitly discussed the circuit design and diode design requirements for picosecond NLTL shock-wave generators and NLTL-driven sampling circuits [31]-[33].

1.3 Contribution of this work

It was mentioned before that SRDs and NLTLs, and other types of circuits by themselves could not provide suitable outputs. However, a combination of avalanche transistors and *SRD*s and NLTLs can produce pulses of high amplitude and narrow pulse width.

Avalanche transistors imply high breakdown voltages to produce a high amplitude pulse. This high amplitude pulse can be used to excite the following *SRD*-based pulse shaping network to sharpen the pulse width.

The *SRD*-based pulse shaping network proposed in this work comprises a parallel diode accompanied by a series one [50]-[56]. The parallel diode is used to shape the rise time. However, the series diode cuts off the pulse sharply and forms the falling edge. This conventional structure suffers from a limited amplitude, which results from the uncoordinated switching time of series and parallel diodes. The source of this imperfection is studied, and a modified configuration is proposed to address the problem. By resolving the issue, the highest possible pulse amplitude is achieved.

It has been established that a pulse with a *dc*-offset is not suitable for radiation through the antenna [56], [57]. The first derivative Gaussian pulse (monopulse) is a *dc*-free pulse appropriate for radiation. The monopulse is usually produced by differentiating the Gaussian pulse. In this study, to achieve a monopulse with the highest possible amplitude, two Gaussian pulses with opposite polarities with a calculated delay are combined using a broadband combiner. The output pulse is a monopulse with high peak power, used to excite the transmitting UWB Vivaldi antenna [58].

The proposed Gaussian pulse transmitters are able to produce a high-power pulse with a narrow pulse width in the range of 200 ps and power of P = 5.78 W. It was achieved by separating two SRDs which allows us to have more accurate control on the output pulse in terms of its an amplitude and a pulse width. Moreover, by using a smart technique based on pulse-shifting, one could obtain a higher power monopulse without using a balun and a differentiator.

Nonlinear transmission lines (NLTLs) are high-impedance waveguides periodically loaded with reverse-biased diodes. These diodes appear as voltage-variable capacitors (varactors) and cause the propagation delay through the NLTL to depend on the wave amplitude. Nonlinearity arises from the voltage-dependent propagation characteristics of the NLTL. Dispersion occurs from the periodicity of the NLTL. Depending on the structure's design (nonlinearity, dispersion, and input waveform), one can generate a variety of waveforms.

The NLTL-based structures are used for generating solitons, which comprise a self-reinforced wave packet that stays unchanged during propagation due to the cancellation of two opposite processes, namely, nonlinearity and dispersion [34].

Many papers have presented the ways of producing ultra-fast pulse generators in the picosecond range. For example, some papers mentioned that they could generate narrow pulses by cascading the unit cells of the NLTLs with reversed biased varactors by using special taping techniques to minimize losses and optimize the output pulse [35]-[40]. Generation of solitons requires a large number of the stages of the NLTLs cascading in the series, which increases the physical sizes and cost of the fabrication. There is a well-known shock-wave concept of generating ultra-fast pulses along with soliton creation. The shock-wave concept considers sharpening the rise and fall time of the pulse by changing the biasing polarity of varactors [41]. Another paper suggested subtracting the opposite polarity branches of the NLTL-based circuit to decrease the fall time of the pulse [42]. In the literature, one can also find a method of utilizing the reflection from the end of the open circuit, which can sharpen both edges of the output pulse [43]. The proposed NLTL-based Gaussian pulse transmitter in this thesis is able to produce a pulse with a narrow pulse width in the range of 175 ps and an amplitude of 12 V.

Chapter II

Avalanche transistors

All the transistors have avalanche behaviour; some are developed to work in the avalanche region. However, the other transistors break in avalanche voltage. Fig. 1 shows a conventional avalanche transistor-based circuit that produces a high amplitude pulse with negative polarity.

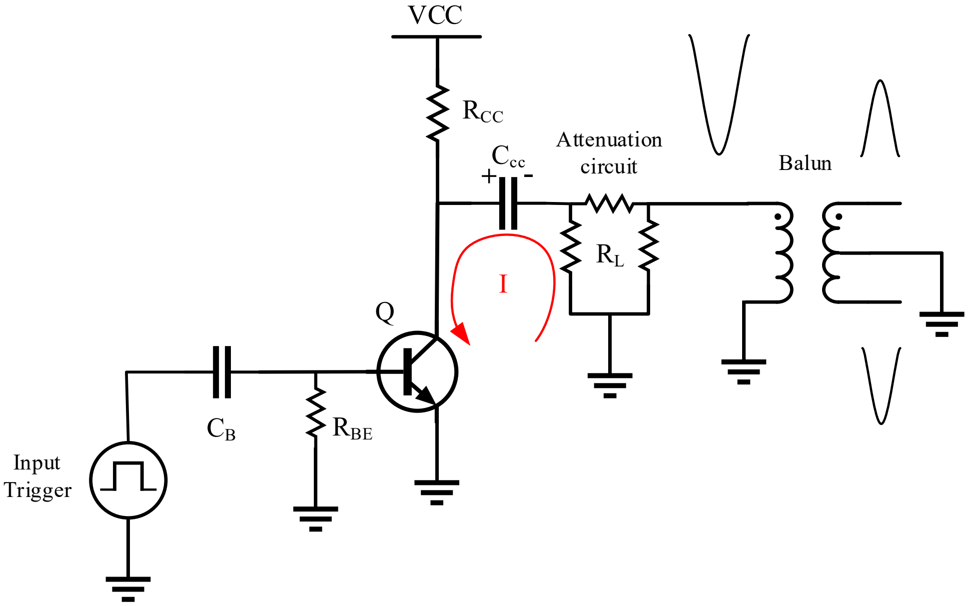

Fig. 1. A schematic of the avalanche-based circuit and a balun.

The circuit consists of an avalanche transistor, *FMMT417*, capacitors (C_{CC}, C_B), resistors (R_{CC}, R_{BE}, R_L), a voltage supply (V_{CC}), and a waveform generator, which is used for generating a trigger pulse that is connected to the base (*B*) of the transistor. The purpose of C_{CC} is to accumulate the charge from the biasing source V_{CC}, while C_B prevents *dc* passing from V_{CC} to the trigger generator. R_{CC} controls the current flow from the V_{CC} to the collector of the transistor. Moreover, R_{CC}

accompanied by C_{CC} determines the time constant of charging C_{CC}. R_{BE} is used to bias the base of the transistor.

Initially, when the input trigger is not presented, the V_{BE} of the transistor is zero, and the transistor is in an off state. A base-emitter voltage of at least 0.7 V is required to turn on the transistor. VCC of equal to BVCER (collector-emitter breakdown voltage with given base-emitter resistor) and a positive trigger pulse of more than 0.7 V are applied to initiate the avalanche process in the circuit. Before the BV_{CER} level is reached, the capacitor C_{CC} accumulates the charge until the trigger appears in the circuit. The charging time constant τ of the RC circuit is as follows [59].

$$\tau = C_{CC}\,(R_{CC} + R_L) \approx C_{CC}\,R_{CC},\ when\ (R_L \ll R_{CC}) \tag{4}$$

In the output, one can see a negative voltage pulse across R_L. A balun is placed at the output of the avalanche-based circuit to convert the negative voltage dropped on the R_L to two opposite pulses. The model of the balun is ADT1-1WT+ with the operational frequency from 0.4 to 800 MHz. The amplitude of the opposite pulses is less than that of the input. These opposite pulses are used to excite the next stage. Notably, the attenuation circuits and balun reduce the amplitude to keep the next stage from damage. When the capacitor is discharged, the avalanche transistor switches to the off state because collector voltage, V_C, drops below BV_{CER}, which means the electric field in the collector-base path cannot maintain the transistor in avalanche mode.

The maximum ratings of the main characteristics of the transistor are as follows: collector-base voltage (V_{CBO}) = 320 V, collector-emitter voltage (V_{CEO}) = 100 V, and emitter-base voltage (V_{EBO})

= 6 V. However, the transistor breaks down and starts working in the avalanche mode when V_{CC} reaches a voltage of more than 100 V. The attenuation circuit in the π-configuration, including R_L, is used to adjust the output amplitude of the circuit if needed. This design uses 8.88 dB of attenuation and 85 Ω of characteristic impedance to decrease the amplitude. The values of the input trigger, biasing voltage of V_{CC}, and all electrical components can be observed in Table I.

TABLE I
THE VALUES OF AVALANCHE-BASED CIRCUIT

Notation	Model/Value	Units
R_{BE}	50	Ω
R_{CC}	54	kΩ
R_L	85	Ω
C_B	0.6	nF
C_{CC}	460	pF
Q	FMMT417	
VCC	302	V
Input Trigger	8	kHz

Overall, there is a trade-off between the output amplitude and the width of the output pulse. By reducing the capacitance value of C_{CC}, a narrow output pulse can be achieved at the cost of lower output amplitude and vice versa. In this design C_{CC} of 460 pF is selected to give optimal amplitude and pulse width for the next stage. Noticeably, the subsequent SRD-based circuit has a maximum tolerable voltage of around 30 volts. C_B and R_{BE} constitute a high pass filter to pass the high-frequency components of the input trigger and sharpen its pulse width.

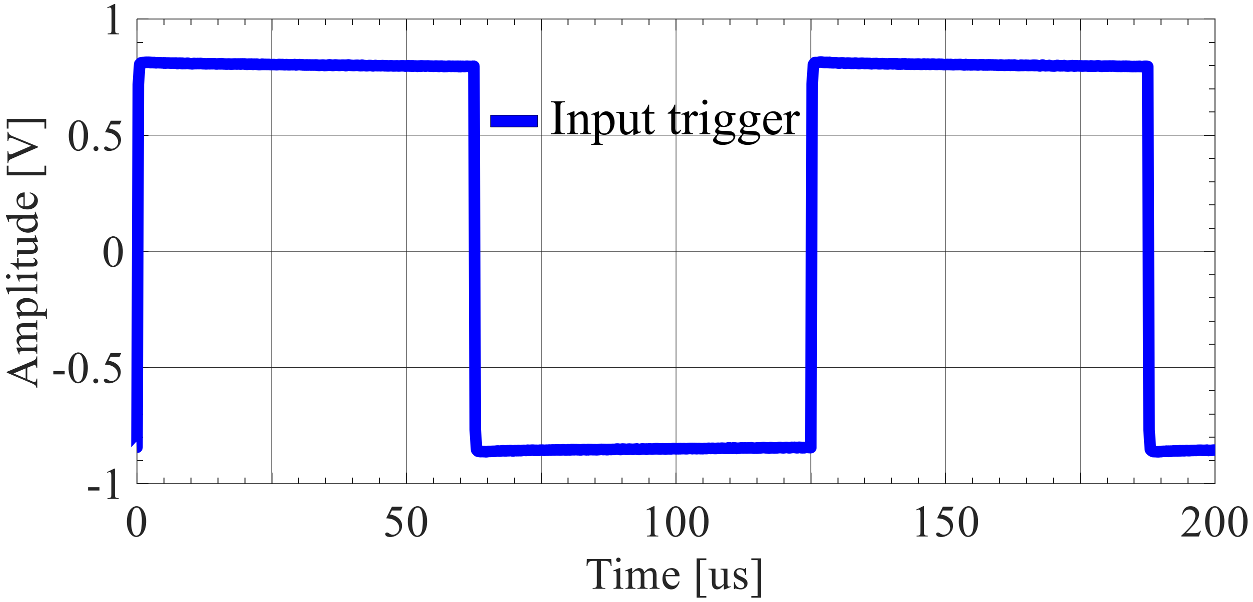

Fig. 2. Input trigger to the avalanche-based circuit.

Fig. 2 shows the input trigger pulse with frequency and peak-to-peak amplitude of 8 kHz and 1.6 V, respectively. The output pulse of the avalanche-based circuit, shown in Fig. 3(a), indicates the amplitude of -270 V, fall time (t_f) of 4.3 ns, and rise time (t_r) of 10.8 ns. Fig. 3(b) shows two oppositely polarized pulses on the outputs of the balun. The parameters of the two pulses after the balun can be seen in Table II.

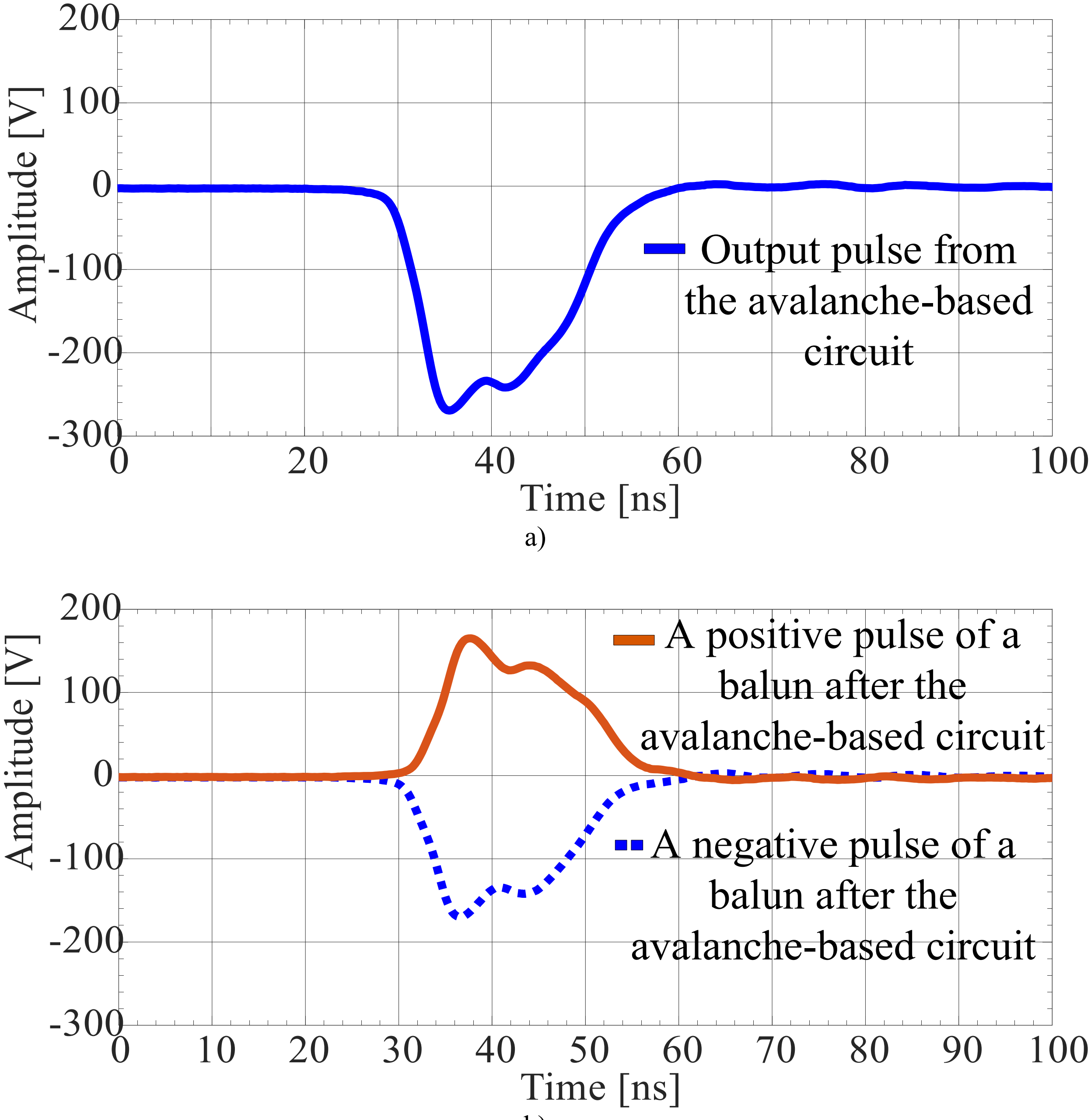

a)

b)

Fig. 3. a) Output pulse from the avalanche-based circuit; b) Positive and negative pulse after the balun.

TABLE II
OUTPUT PARAMETERS OF AVALANCHE-BASED CIRCUIT

Parameter	Output before balun	Positive pulse after balun	Negative pulse after balun	Units
Amplitude	-270	165	-170	V
t_r	10.8	4.5	15.5	ns
t_f	4.3	16	4.5	ns

The high-power pulse generator is realized on *RO4003C* with dielectric permittivity (ε_r) of 3.38, dielectric substrate thickness (h) of 0.81 mm, and copper thickness (t) of 18 µm.

Chapter III

SRD Based Pulse-Shaping Circuits

The next stage of the high-power transmitter is an *SRD*-based pulse-shaping circuit. A conventional diode is made of two semiconductors that constitute a *PN* junction. To develop a conventional diode for fast switching applications, a thin intrinsic layer is dopped between the two “p” and “n” type semiconductors. The intrinsic layer represents a small and constant capacitive behaviour in the reverse biasing stage [56]. The *SRD*s are characterized by having a high breakdown voltage in reverse bias [53]. Generally, a diode experiences a recovery time when switching from *ON* to *OFF* states. The recovery time is the time taken by a diode to cease the current completely.

In contrast to a conventional diode, which is gradually switched off during the recovery time, an *SRD* goes to off state abruptly [57]-[59]. Fig. 4 is an illustration of the reverse recovery behaviour of a diode in switching from *ON* to *OFF* states for a conventional diode and an SRD separately with a positive biasing voltage and a negative Gaussian input pulse. According to Fig. 4, the reverse recovery time of an SRD has three different segments: ramping time, fast transition time, and rounding off. The ramping segment is a stage needed for a diode to prepare for a sharp jump, and it is determined by the forward and reverse currents of the diode [53]. Among these three segments, fast transition time is of interest to produce sharp rising/falling edges. Table III shows the main specifications of the SRD model MP4033, where t_t is the fast transition time, t_L is an operational period, and f_{max} is a maximum operating frequency.

TABLE III
THE SPECIFICATION OF THE DIODE, MODEL MP4033 FROM M-PULSE MICROWAVE

The breakdown voltage V_{br} (min) ($I_r = 10\ \mu A$)	t_l	t_L	f_{max}
30 V	70 ps	30 ns	14 GHz

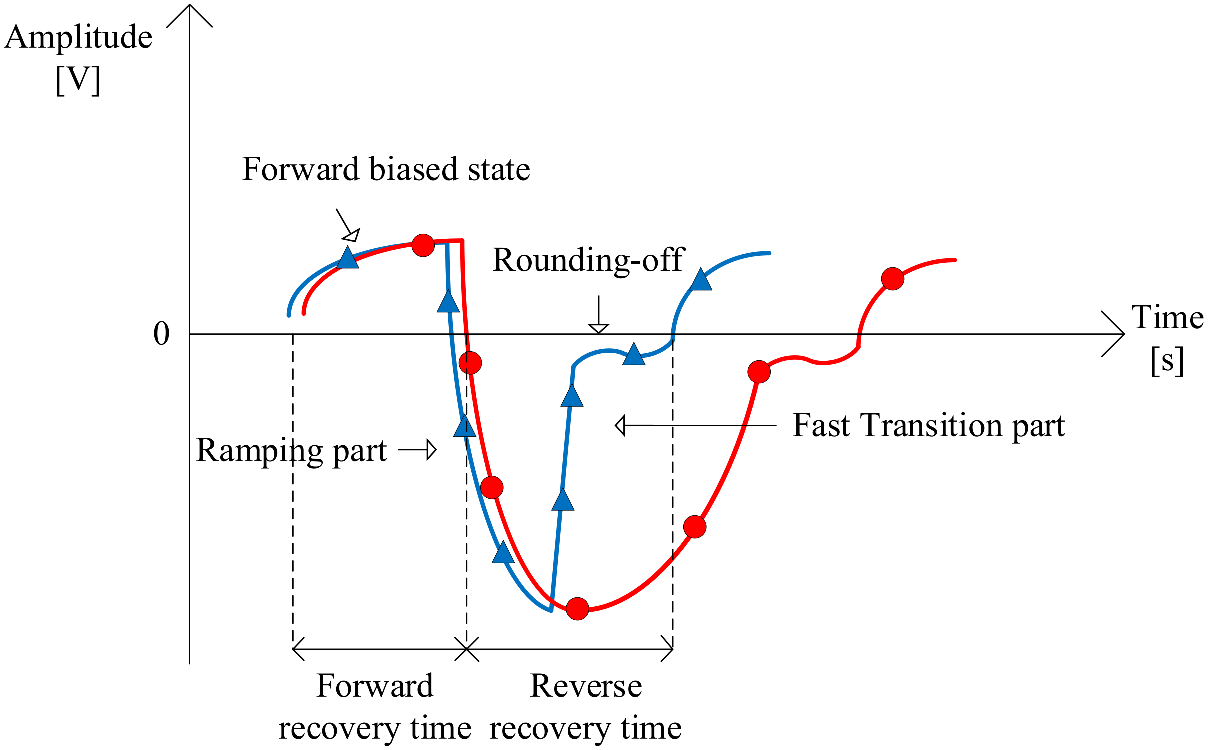

Fig. 4. Representation of reverse recovery time.

3.1 Proposed modified SRD Based Pulse-Shaping Circuit

The *SRD*s are suited for shaping ultra-fast Gaussian pulses with a pulse width in the sub-nanosecond range for microwave and *RF* applications. In past decades, the literature has mentioned various circuit configurations with *SRD*s. Fig. 5(a) shows a conventional structure that comprises a parallel *SRD* followed by a series one [50]. The parallel *SRD* is used to sharpen the rising edge, whereas series one shapes the falling edge. The forward and reverse currents of the series diode are controlled by the voltage drops on the anode of the parallel diode. Hence, the series diode imposes a limitation on the output amplitude. Fig. 5(b) reveals a structure using an *SRD*, a Schottky diode (*SD*), and a delay line. This configuration works based on an incident sharp pulse produced by the *SRD,* added to its reflected pulse across the delay line [59], [64]. Although the configuration with a delay line does not have limitations from the series diode, it lucks from the tunability during the measurements.

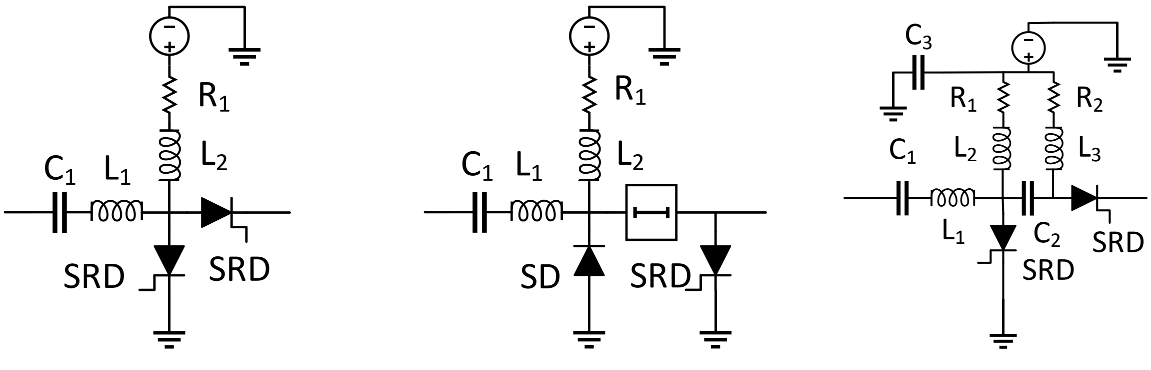

a) b) c)

Fig. 5. Different configurations of SRD based pulse-shaping circuit: a) A shunt and series configuration of SRDs; b) A delay-based shaping network; c) Improved design of the pulse shaping network with the shunt and series configuration of SRDs.

This work proposes a new configuration of a series and parallel *SRD*s, as shown in Fig. 5(c), to improve the amplitude of the Gaussian output pulse. Based on this configuration, biasing of the series diode is separated using a capacitor and an extra biasing network, including an extra resistor and an inductor. Introducing a capacitor between two *SRD*s enables control of a biasing current for each *SRD* separately. Hence, a higher amplitude can be achieved compared to a conventional configuration. The component values of the proposed circuits are as follows: $R_{1,2}$=333 Ω, L_1= 9.5 nH, $L_{2,3}$=100 nH, C_1=1 nF, C_2=13 nF, and C_3=1 μF. The Gaussian pulses produced by the conventional *SRD*-based pulse-shaping circuit without a capacitor are shown in Fig. 6(a), driven by the input pulse shown in Fig. 3(b). This figure shows that an amplitude of around ±12 V for positive and negative pulses with a pulse width of 148 ps is achieved. The improved output results of the *SRD* based pulse-shaping circuit of Fig. 5(c) are presented in Fig 6(b). The positive pulse has an amplitude of 26.3 V and a pulse width of 165 ps, while the negative pulse has an amplitude of -27.65 V and 170 ps. Fig 6(c) shows a normalized spectrum of the pulses from Fig 6(b).

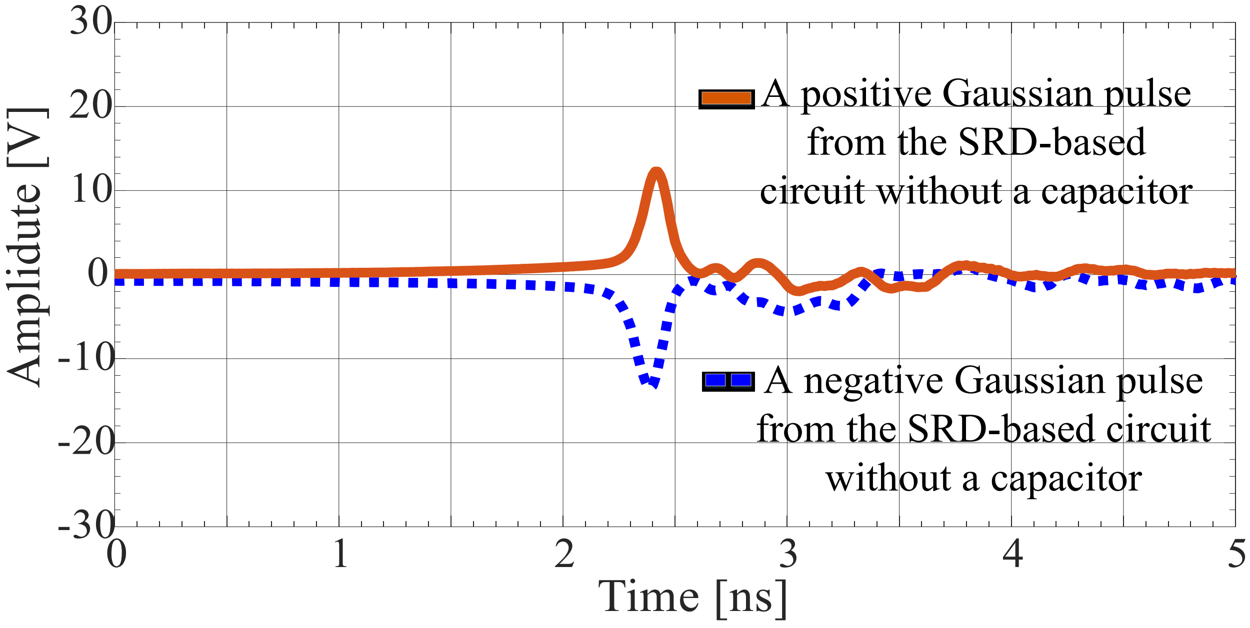

a)

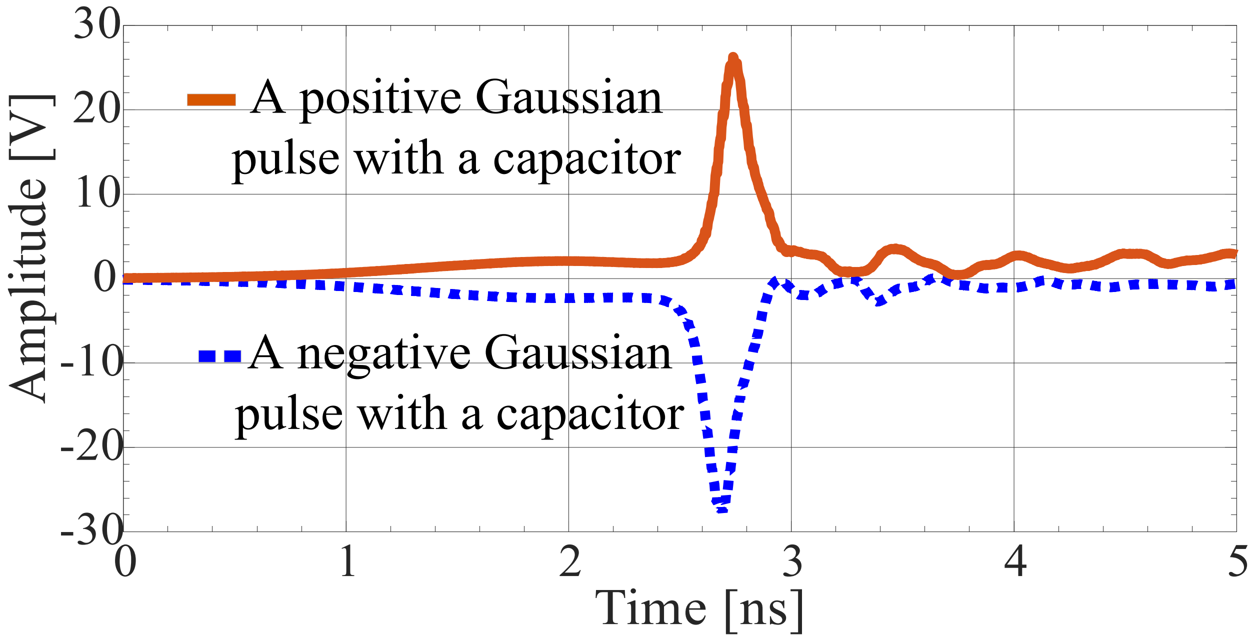
30
20
10
0
-10
-20
-30
Amplitude [V]
0
1
2
3
4
5
Time [ns]
A positive Gaussian pulse with a capacitor
A negative Gaussian pulse with a capacitor

b)

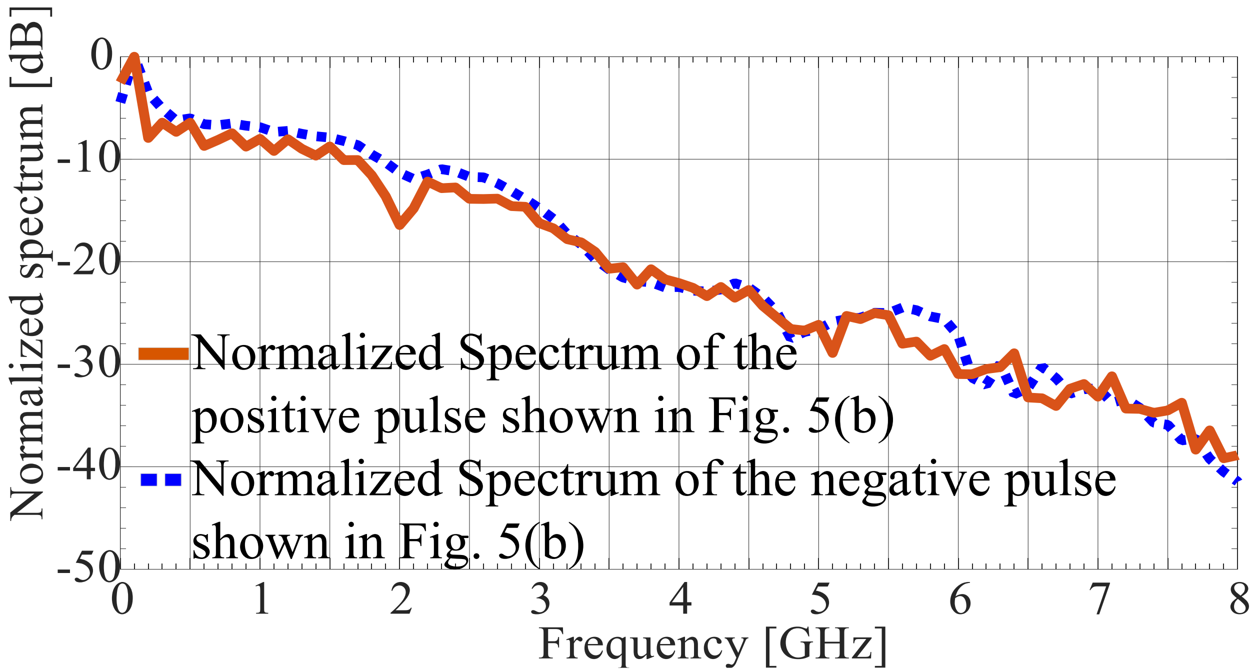
0
-10
-20
-30
-40
-50
Normalized spectrum [dB]
0
1
2
3
4
5
6
7
8
Frequency [GHz]
Normalized Spectrum of the positive pulse shown in Fig. 5(b)
Normalized Spectrum of the negative pulse shown in Fig. 5(b)

c)

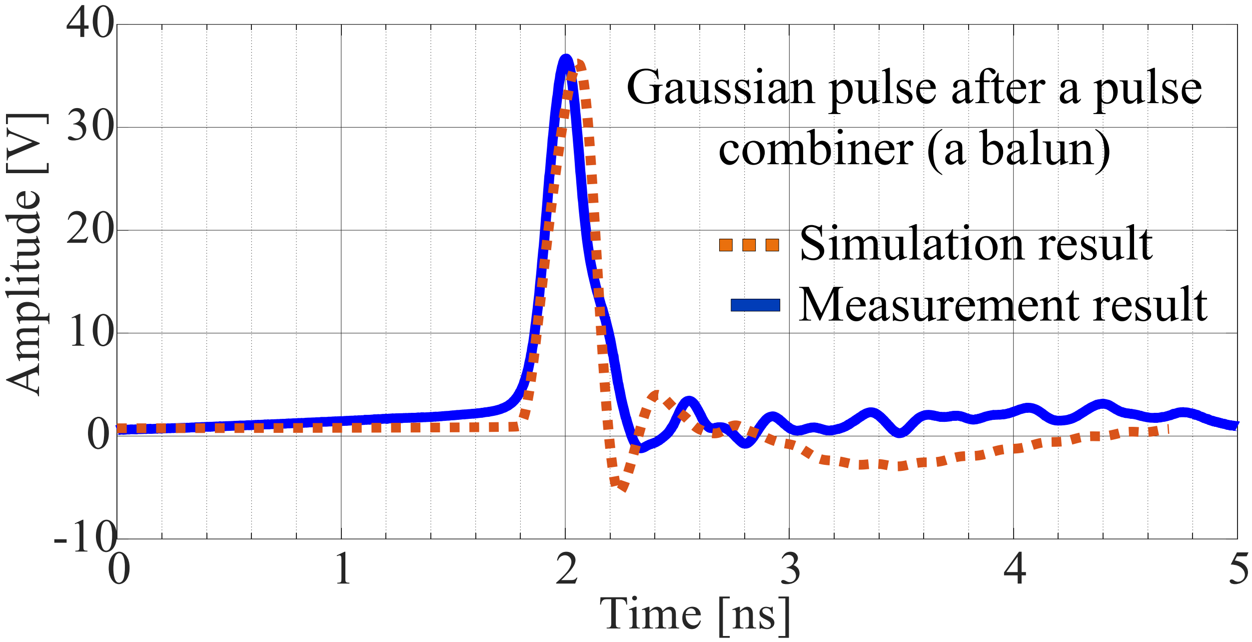

d)

Fig. 6. a) Gaussian pulses from the SRD based pulse-shaping circuit without capacitor; b) Gaussian pulses from the improved SRD based pulse-shaping circuit; c) Normalized spectrum of Gaussian pulses from the improved SRD based pulse-shaping circuit; d) Gaussian pulse after a pulse combiner (a balun).

3.2 Conventional Monopulse Shaping network using balun and Differentiator

Gaussian pulses of two branches shown in Fig. 6 (b) have opposite polarities. A balun of broadband operation, model (*TC1-1-43A+*) with a frequency operation of 650 to 4000 MHz, is used to subtract these two opposite pulses and create a Gaussian pulse of higher amplitude than a single branch. In Fig. 6(c), one can observe a normalized spectrum of Gaussian pulses from the improved SRD based pulse-shaping circuit. Fig. 6(d) shows the output pulse of the balun with pulse width and amplitude of 200 ps and 36.7 V, respectively. The experimental results align well with the Advanced Design Systems (ADS) simulation results. The Gaussian pulse of Fig. 6(d) is not a *dc*-free pulse. Thus, it needs a monopulse shaping network or a differentiator. A differentiation process can be accomplished using a 90˚ coupler [56], [57], which creates a monopulse. The monopulse is the first derivative Gaussian pulse, having no *dc* component. The monopulse shaping network (balun) model used in this test is TCM1-83X+ from Mini-Circuits®, with an operating frequency range from 10 to 8000 MHz. The whole configuration of the transmitter is shown in Fig. 7.

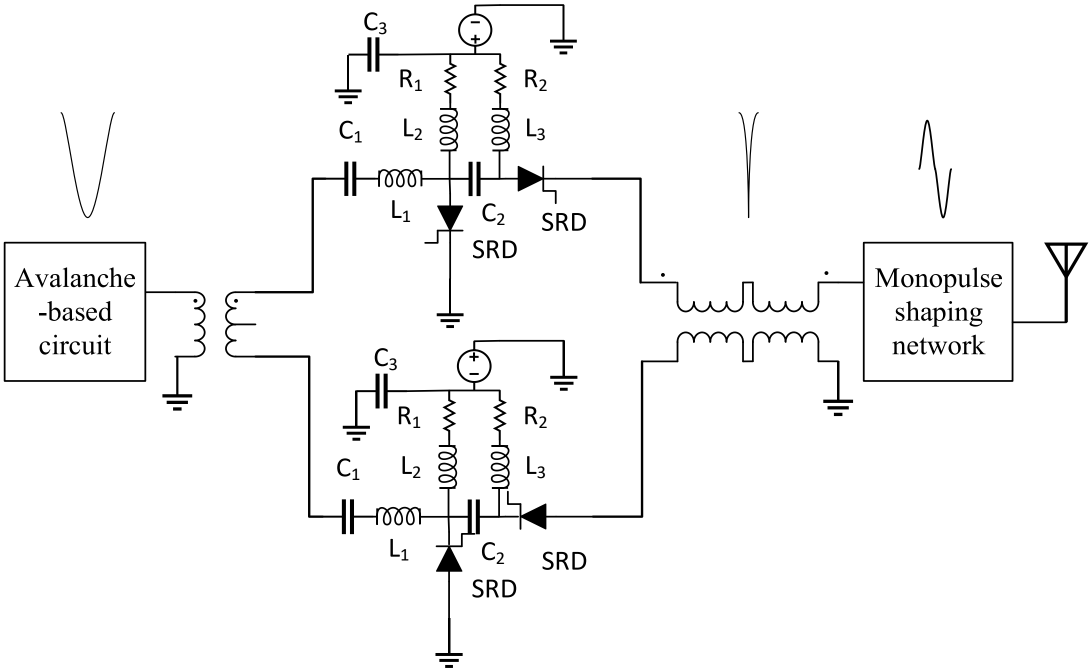

Fig. 7. The schematic of the SRD based pulse-shaping circuit with a balun and Differentiator.

This system includes an avalanche-based circuit, a Gaussian pulse shaping network, a balun, a 90˚ coupler as a monopulse converter, and an antenna.

A 90˚ coupler with a lower cutoff frequency at about 1 GHz is used to convert the Gaussian pulse of Fig. 6(d) to a monopulse [52], [53]. Fig. 8 shows the output monopulse with amplitudes of +14.2 V and -11.75 V ($V_{P\text{-}P}$ = 25.96 V) and pulse widths of 192 ps and 264 ps, respectively.

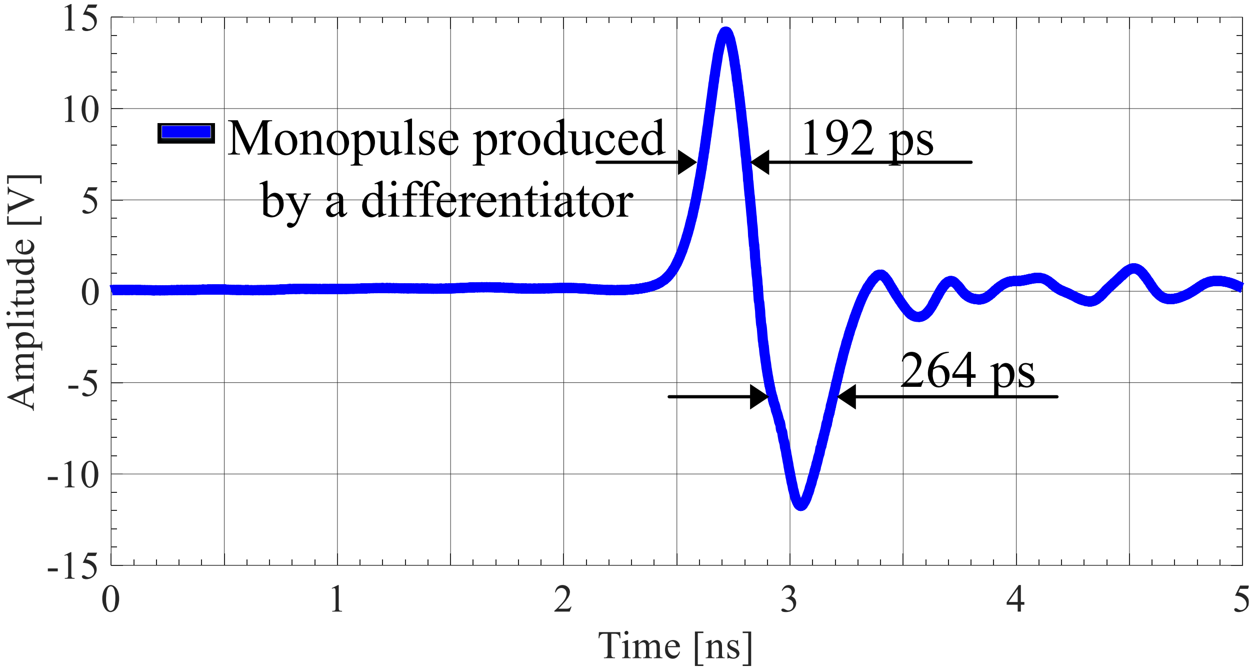

Fig. 8. A monopulse produced by a differentiator (without improvement).

The spectrum of this pulse is shown in Fig. 9. A -10 dB bandwidth of this pulse is roughly from 0.2 GHz to 2.3 GHz. This pulse suffers from an asymmetry in amplitude and pulse width between its positive and negative parts. The average peak power of 3.37 W is achieved. The following section introduces another approach to increasing the amplitude and enhancing pulse symmetry.

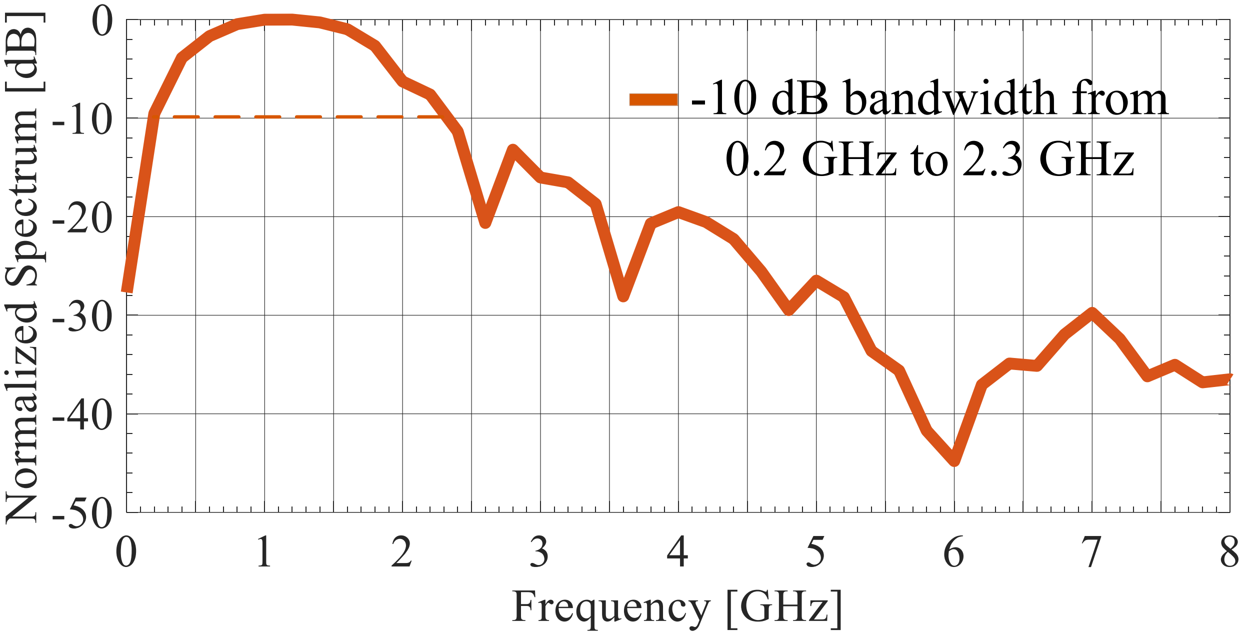

Fig. 9. Normalized spectrum of the pulse.

3.3 Proposed procedure of generating the monopulse

In this design, two parallel branches provide two opposite polarities with high amplitude and low pulse width. In order to improve the amplitude, pulse width, and symmetry of the output pulse, a possible procedure is to prepare an appropriate time delay for the first branch, then add the pulse of the other branch to the time-shifted pulse of the first branch. Fig. 10 depicts the summation procedure of two distinct pulses with opposite polarities. According to Fig. 10, a combiner with a bandwidth consistent with the pulse bandwidth shown in Fig. 6(c) is needed. Fig. 11 shows the frequency response of a broadband combiner with a -10 dB bandwidth of *dc* to more than 12.5 GHz.

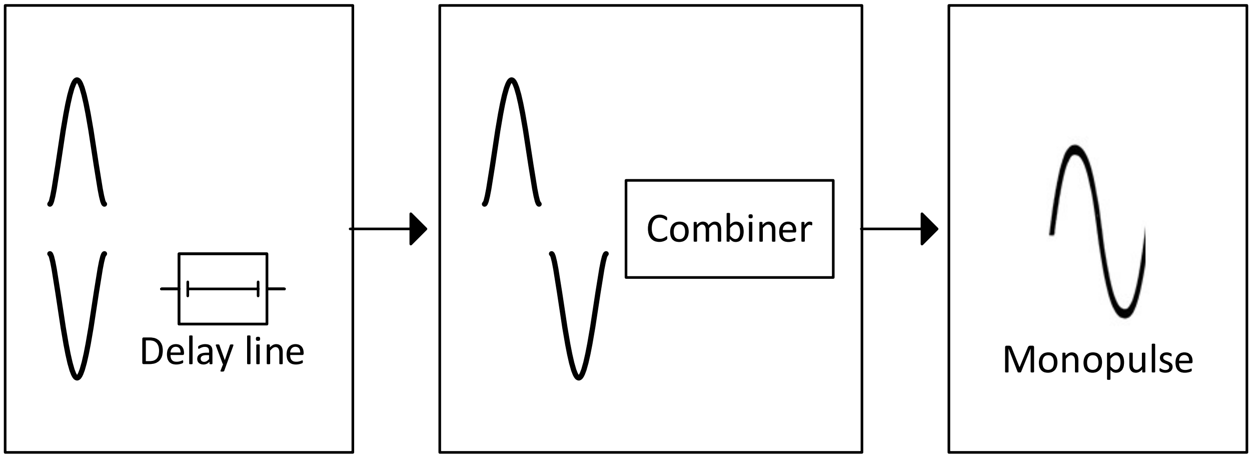

Fig. 10. Pulse-shifting technique for a monopulse creation.

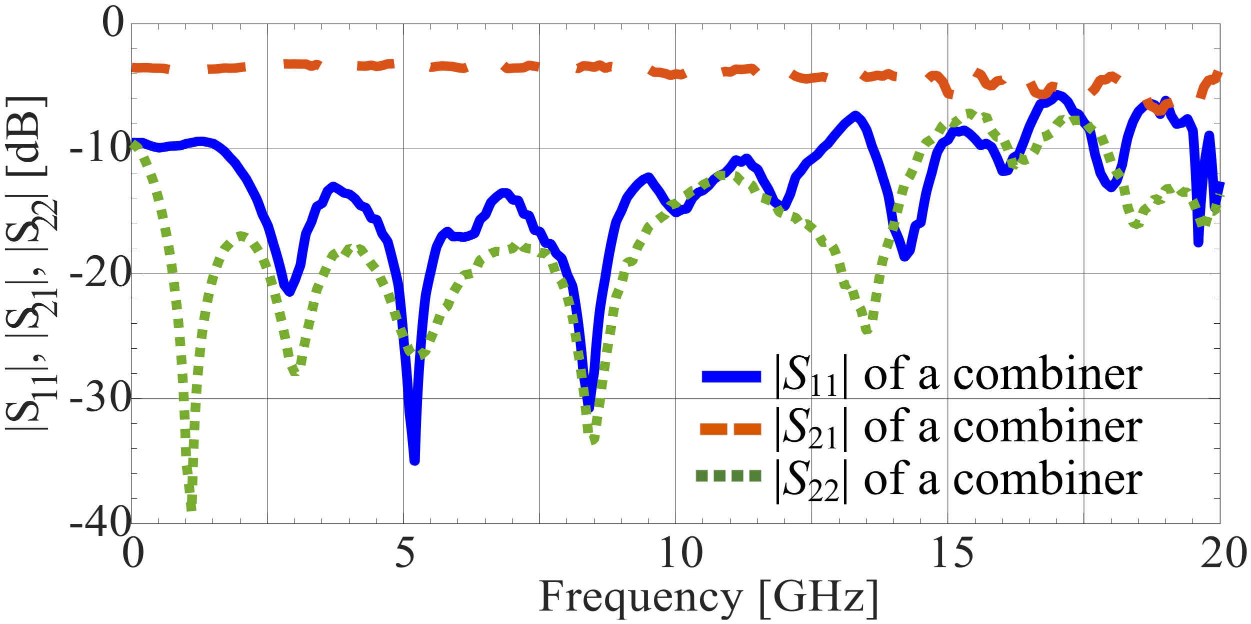

Fig. 11. S-parameters of a combiner of the port 2.

Fig. 12 shows the schematic of the whole proposed monopulse shaping network. The fabricated system is shown in Fig. 13, which is excited using the square pulse of Fig. 2. The measured output of this design is a monopulse of low ringing level, high amplitude, and proper pulse width for an imaging application. Fig. 14 shows the monopulse with positive pulse width and amplitude of 174 ps and 17.08 V, respectively. As for the negative part of the monopulse, pulse width and amplitude of 169 ps and -17.1 V, respectively, are obtained with a 50Ω load. Therefore, the output monopulse presents a peak-to-peak voltage of 34.18 V with a peak power of 5.87 W.

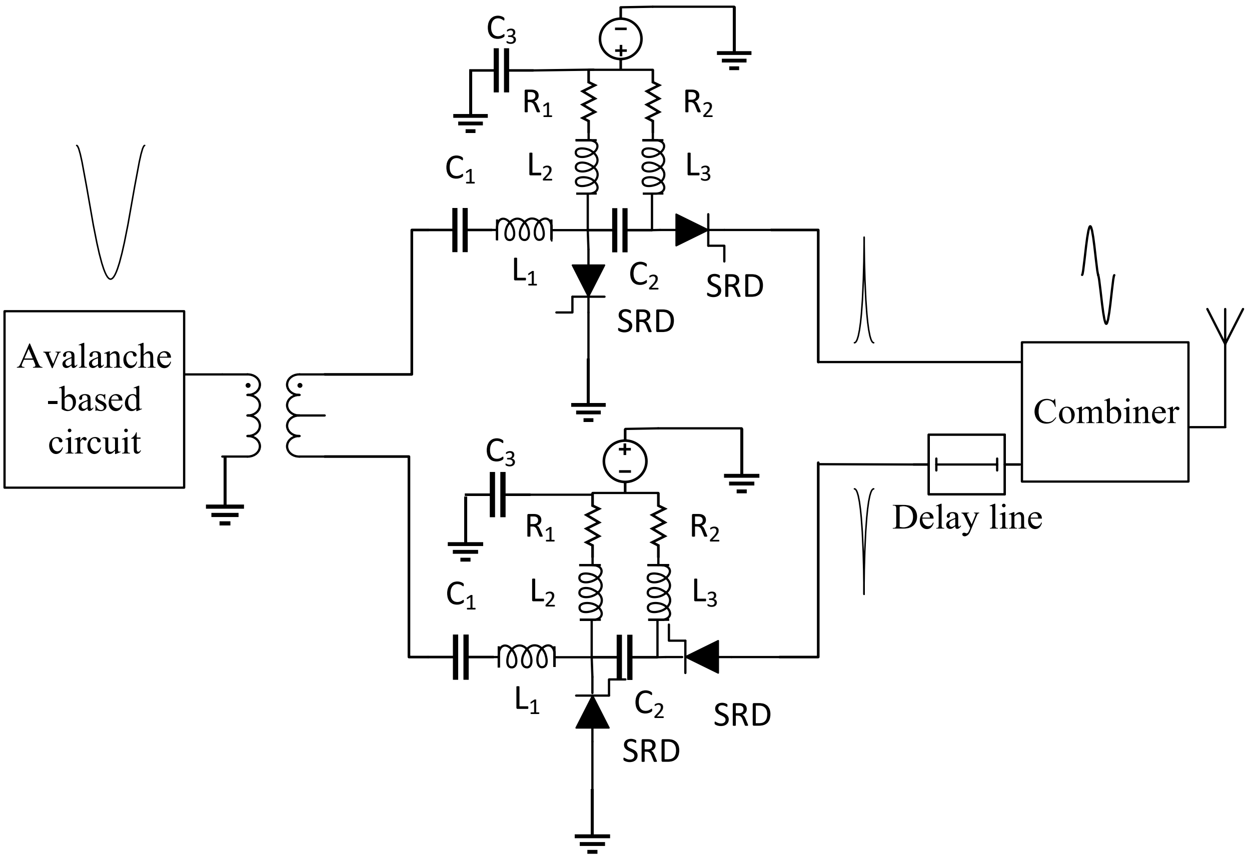

Fig. 12. Schematic of a complete circuit.

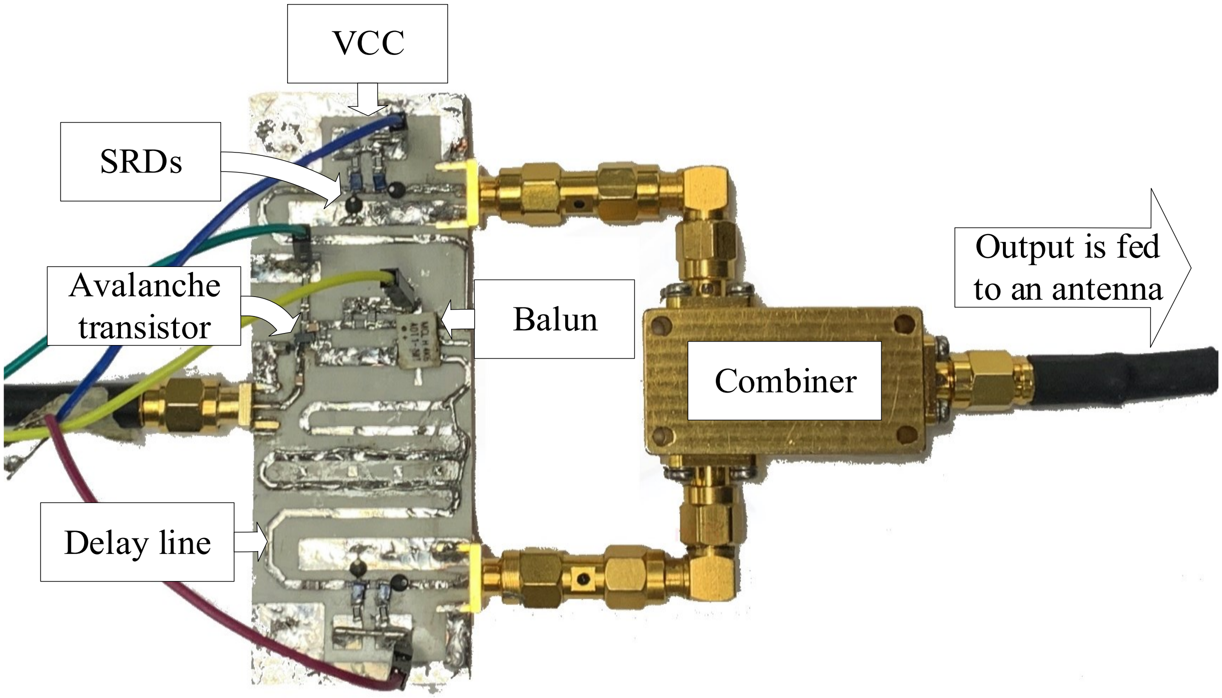

Fig. 13. Fabricated circuit of a complete high-power transmitter.

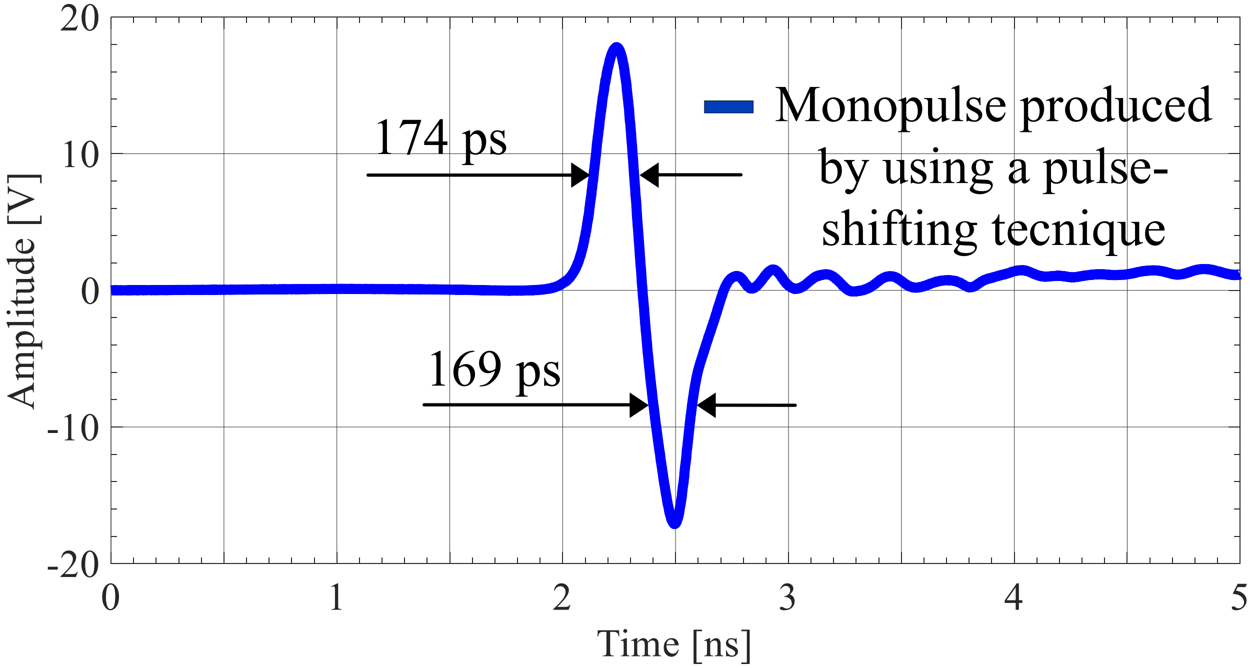

Fig. 14. Monopulse produced by using a pulse-shifting technique.

Fig. 15 shows the -10 dB bandwidth of this pulse. Note that there is a trade-off between the pulse width and amplitude of the monopulse; by tuning either the charging capacitor or the bias voltage, a peak-to-peak amplitude of around 40 V and a pulse width of 200 ps can be achieved.

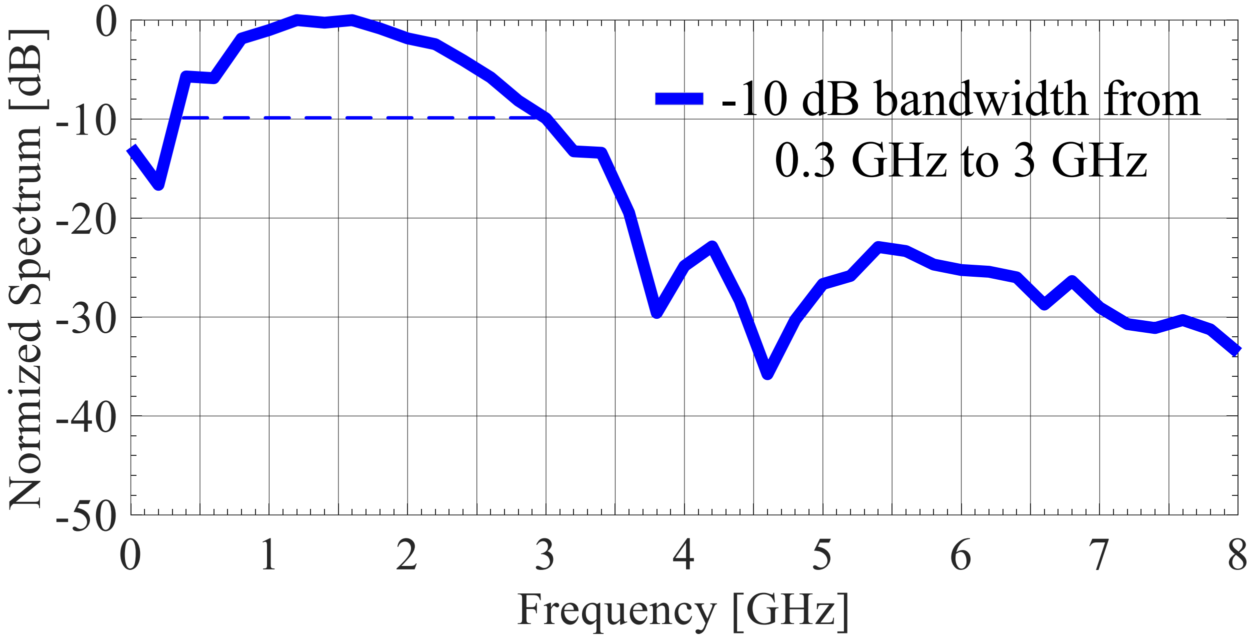

Fig. 15. Normalized spectrum of the pulse.

Fig. 16 shows the comparison between pulses in terms of a normalized spectrum. This design shows superior characteristics over the previous design, having -10 dB bandwidth from 0.3 GHz to 3 GHz compared to the previous design of Fig. 9, with -10 dB bandwidth from 0.2 GHz to 2.3 GHz.

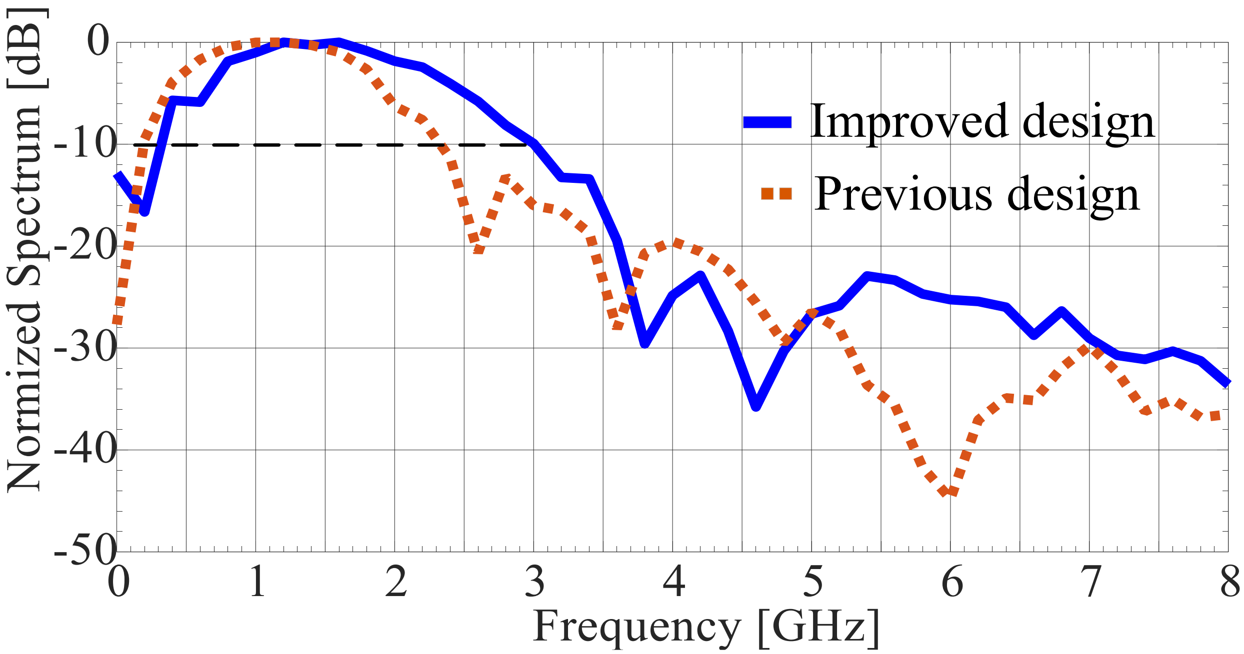

Fig. 16. Comparison between the improved design and the previous design.

Table IV illustrates a detailed summary of the comparison of this work with previous publications. In [50], the Gaussian pulse has an amplitude of 0.7 V and a pulse width of 94 ps. In [56], measurement results illustrate a Gaussian pulse with an amplitude of 0.83 V and a pulse width of 153 ps. The monopulse specifications of [56] are 0.34 V of amplitude and 126 ps of the pulse width. In the design in [57], the output pulse has an amplitude of 6.8 V and a pulse width of 173 ps. The monopulse specification of [57] is 2.8 V of amplitude and 220 ps of the pulse width. Moreover, [59] and [64] elaborate on another method of generating narrow Gaussian pulses using the delay line-based technique. In [59] and [64], Gaussian pulse amplitudes of around 26 V and 34.5 V and pulse widths of 140 ps and 155 ps are reported.

TABLE IV
COMPARISON BETWEEN THE PERFORMANCES OF THE IMPROVED
SRD PULSE-SHAPING CIRCUIT AND SOME PREVIOUSLY PUBLISHED GAUSSIAN PULSE GENERATORS

Ref.	Pulse Shaping	Amplitude of the		FWHM (ps)	
		Gaussian pulse (V)	Monopulse (V)	Gaussian pulse	Monopulse
[50]	SRD-Based	0.7	-	94	-
[56]	SRD-Based	0.83(1.67)	0.34(0.14)	153(214)	126(99)
[57]	SRD-Based	6.8	2.8(-2.1)	173	220
[59]	Delay line	34.5	-	155	-
[64]	Delay line	25(26)	-	140(135)	-
This work	SRD-Based	36.7	-	193	-
		26.3(-27.65)	17.08(-17.1)	165(170)	174(169)

The design in the current study has superior characteristics over those from previously published works in terms of amplitude for high-depth penetration applications. The output result of this work is a monopulse with a peak-to-peak amplitude of more than 34 V and a pulse width of around 170 ps. Fig. 17 shows a diagram of the complete system.

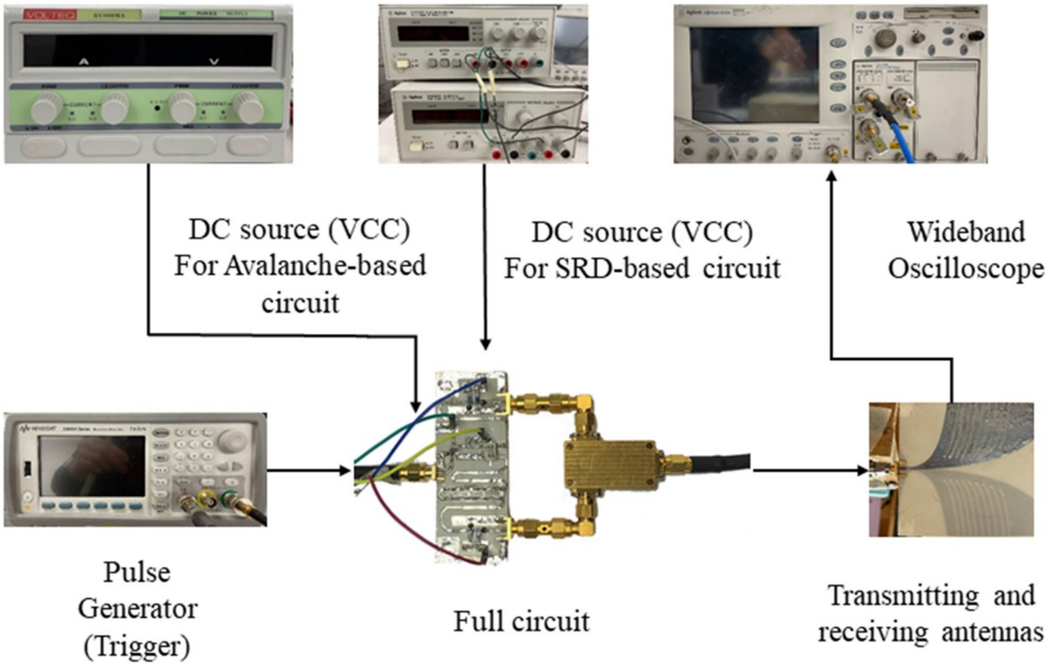

Fig. 17. Diagram of the complete system.

3.4 Experimental testing in the air

The monopulse in Fig. 14 is fed to a transmitting Vivaldi antenna, shown in Fig. 18, used to radiate the pulse through the medium for imaging purposes. Fig. 19 indicates that the antenna has a -10 dB bandwidth of 0.9 GHz to 12 GHz. The output pulse, the second derivative Gaussian pulse, is captured by a receiving Vivaldi antenna located 12 cm from the transmitting antenna. The pulse from the receiving antenna can be seen in Fig. 20. This pulse has a pulse width of 164 ps, which is proper for a range resolution of less than 2.5 cm in the air.

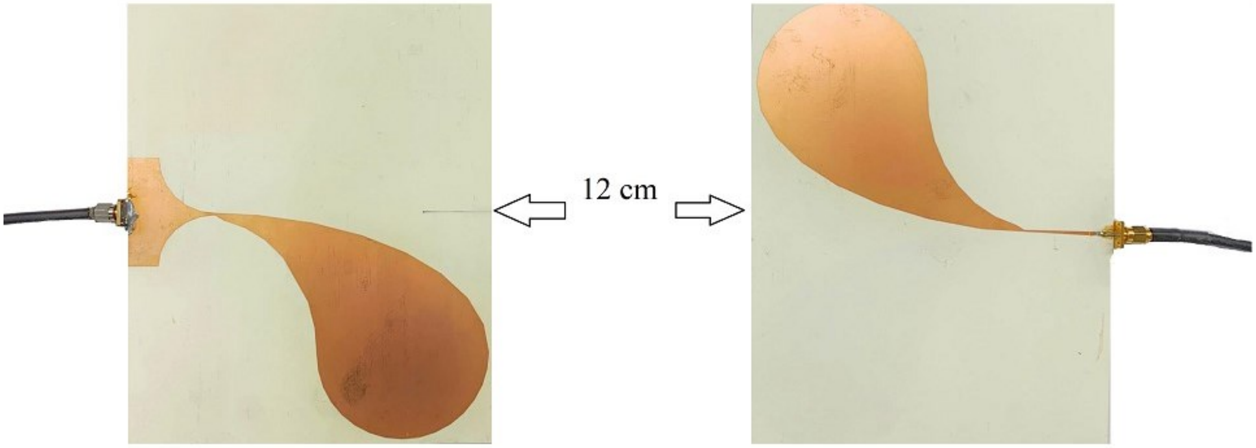

Fig. 18. Vivaldi antennas used for testing a monopulse in the air.

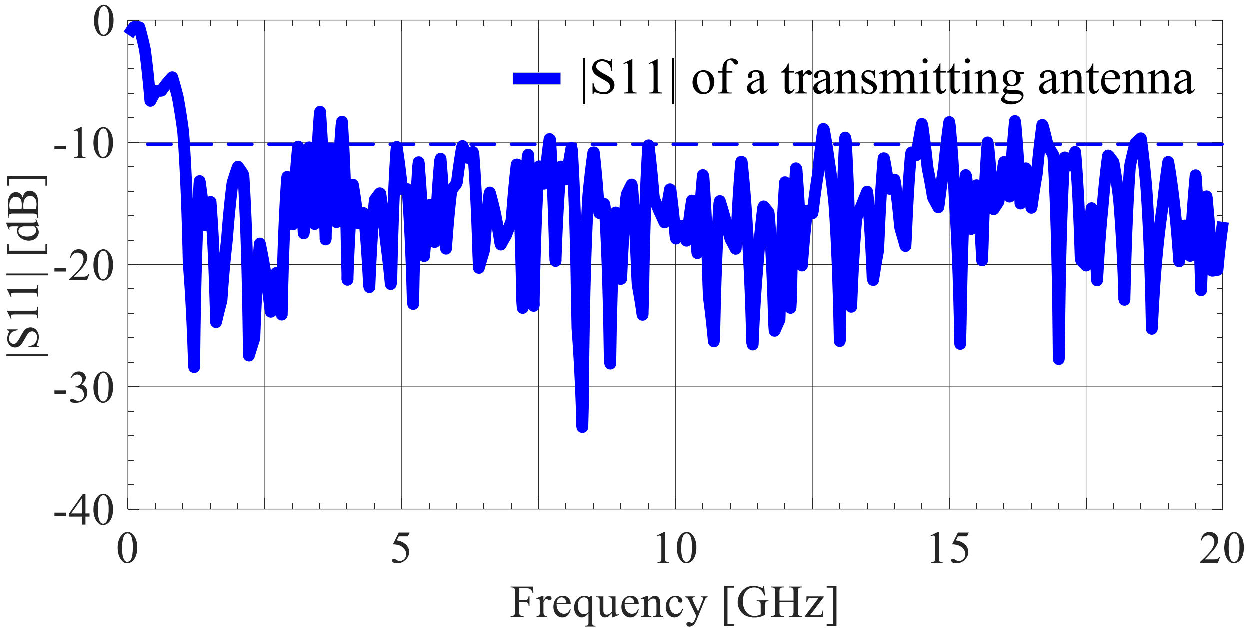

Fig. 19. |S11| of a transmitting antenna.

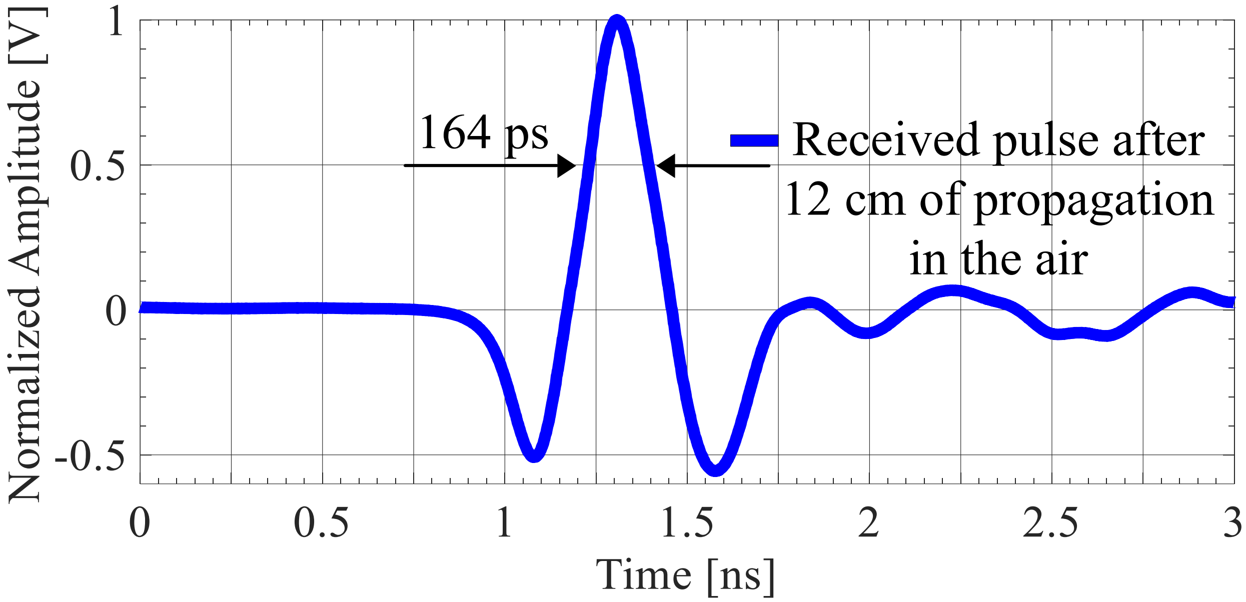

Fig. 20. Normalized the second derivative Gaussian pulse from the receiving Vivaldi antenna with a pulse width of 164 ps.

3.5 Experimental verification of the system

In order to verify the system, various imaging experiments were conducted. One of them is a buried metal object in the sand. Fig. 21(a) and Fig, 21(b) show the geometry of the transmitting antenna (receiving antenna is identical), the experimental setup, and the geometry of the buried object. The transmitting and receiving antennas are placed parallel with around 4 cm spacing to avoid a high mutual coupling. The data is collected in a C-scan configuration with 2 cm increments in both x and y directions. The number of the aperture positions is 25 on both x and y axes. In these measurements, the number of pulses used for averaging is 16. A python script code automates the measurement to move the antennas along the required aperture, and then the data is saved on a high frequency sampling oscilloscope. Fig. 22 illustrates the reconstructed images of the buried object in the depth of 26 cm and 40 cm, respectively. Thus, our system is complete and ready to use for imaging applications.

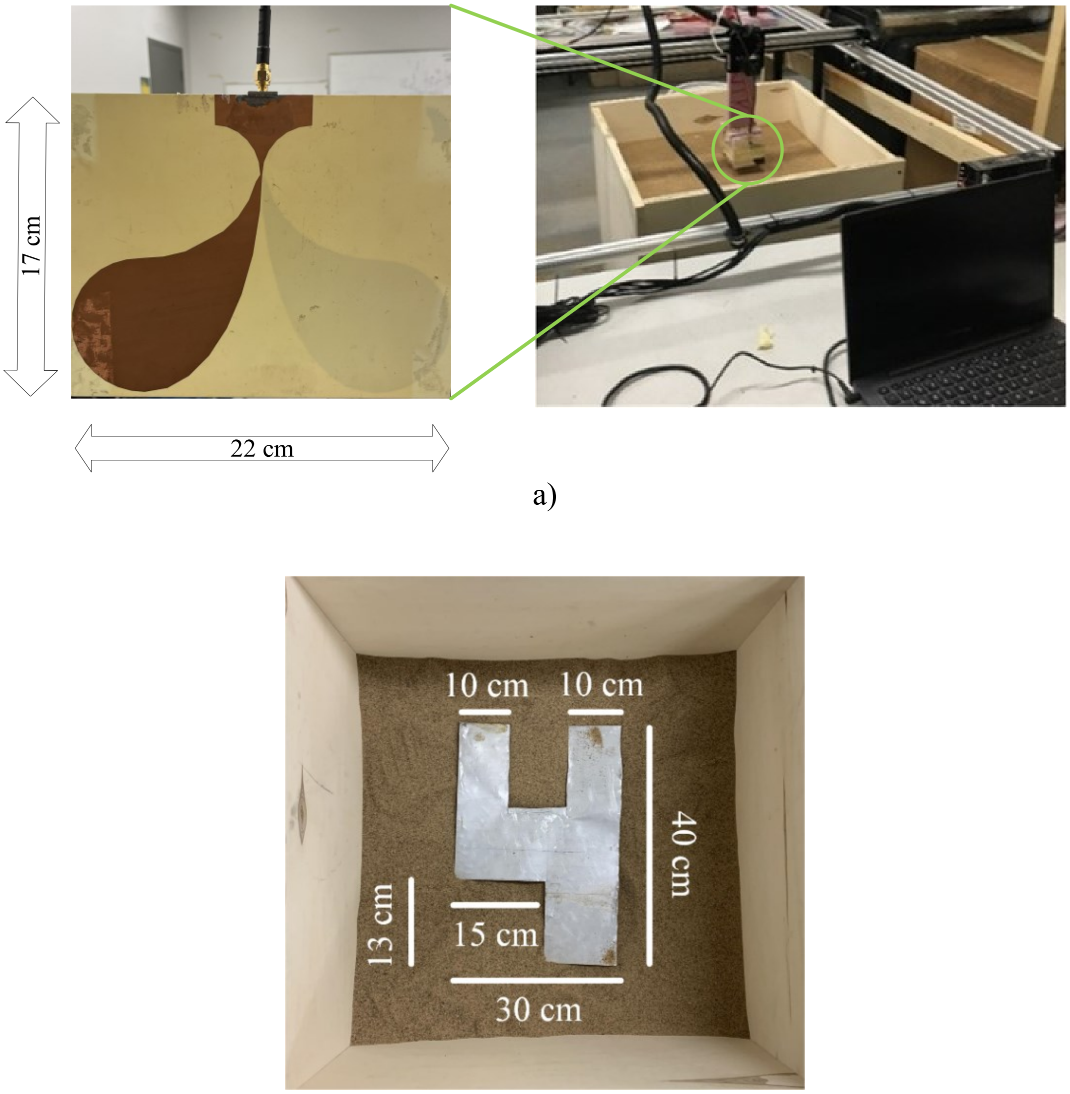

a)

b)

Fig. 21. a) Experimental setup; b) Top view of the buried object.

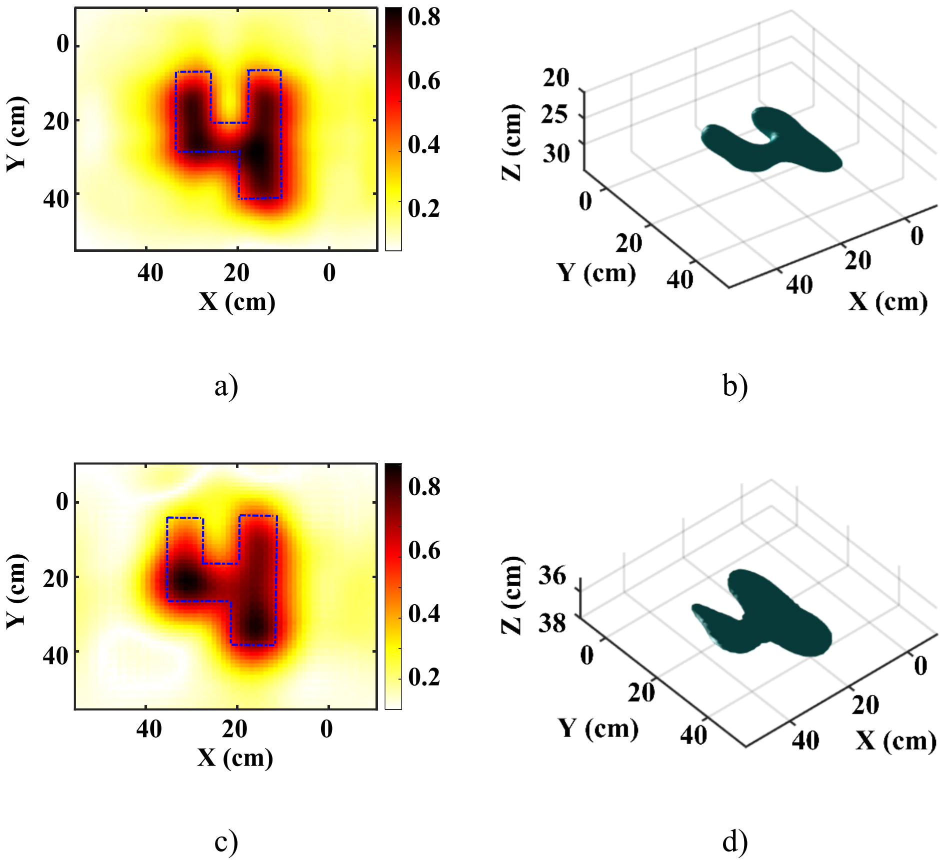

Fig. 22. Reconstructed images: a) Image cross section at z=-26 cm; b) Isosurface 3D image; c) Image cross section at z=-40 cm; d) Isosurface 3D image.

The depth resolution of the proposed system is equal to $\frac{c\tau}{2\sqrt{\varepsilon_{sand}}} = \frac{3\times10^{10}(cm/\sec)\times164ps}{2\sqrt{2.6}} = 1.5\ cm.$

3.6 Conclusion

A high-power Gaussian pulse transmitter for imaging applications was proposed and fabricated in this paper. The transmitter consists of four main parts: an avalanche transistor-based circuit, an SRD-based pulse-shaping network, a broadband combiner, and Vivaldi antennas. Moreover, the application of our system was tested successfully and can be used for any imaging application.

In this work, the avalanche-based circuit is developed by using the avalanche transistor with a high breakdown voltage for creating a high amplitude Gaussian pulse. The output pulse of the avalanche-based circuit has an amplitude of 270 V. The next stage of the circuit is a balun which divides the output pulse into two reverse polarity pulses with an amplitude of 165 V and -170 V.

The SRD based pulse-shaping circuit is developed to sharpen the rising and falling edges of the output pulses. It is carried out by separating two SRDs with a capacitor that blocks *dc* from the first SRD to the second SRD. As a result, the forward current of each SRD is controlled separately. The output pulses have amplitudes of 26.3 V and -27.65 V with pulse widths of 165 ps and 170 ps, respectively.

A high-power monopulse is produced by implementing the pulse-shifting technique. In fact, by delaying a negative Gaussian pulse and combining it with a positive Gaussian pulse, we recorded a monopulse of the peak-to-peak voltage of 34.18 V with a peak power of 5.87 W. The positive part of the monopulse has an amplitude of 17.08 V and a pulse width of 174 ps. The negative part of the monopulse has an amplitude of 17.1 v and a pulse width of 169 ps.

After transmitting through a Vivaldi antenna, the monopulse becomes the second derivative Gaussian pulse when propagating in the medium. After propagating 12 cm in air, the received pulse has a pulse width of 164 ps. As can be seen, it is perfect for high resolution and high depth imaging applications.

Finally, the designed high-power transmitter is validated for a high-depth microwave imaging application. An imaging experiment is conducted with the buried objects up to depths of 40 cm. The reconstructed images show the buried object’s shape, orientation, and estimated dimensions, and the 3D images with the depth resolution of 1.5 cm confirm the functionality of the designed transmitter.

Chapter IV

Nonlinear Transmission Line Theory

The Nonlinear Transmission Line (NLTL) is a nonlinear, dispersive, and lossy network. Frequency-dependent losses arise from the resistance of a diode (R_d) and skin-effect losses. The periodic structure is an undesired low-pass filter with a cutoff (Bragg) frequency (ω_{Bragg}). The variable diode capacitance introduces the desired reduction in propagation delay with increasing reverse bias, reducing the fall time of waves propagating on the NLTL [31]. The schematics of the NLTLs are shown in Fig. 23. From Fig. 23, one can see that the lumped model of the NLTL is represented as an inductor in series and a capacitor in parallel. Since varactors have a variable capacitance, the total capacitance is a sum of the average capacitance of the varactor and a parasitic capacitance created by the NLTLs. The distributed model is represented as a transmission line along which the pulse propagates and a shunt varactor, which contributes to the nonlinearity of the NLTLs due to the variable capacitance.

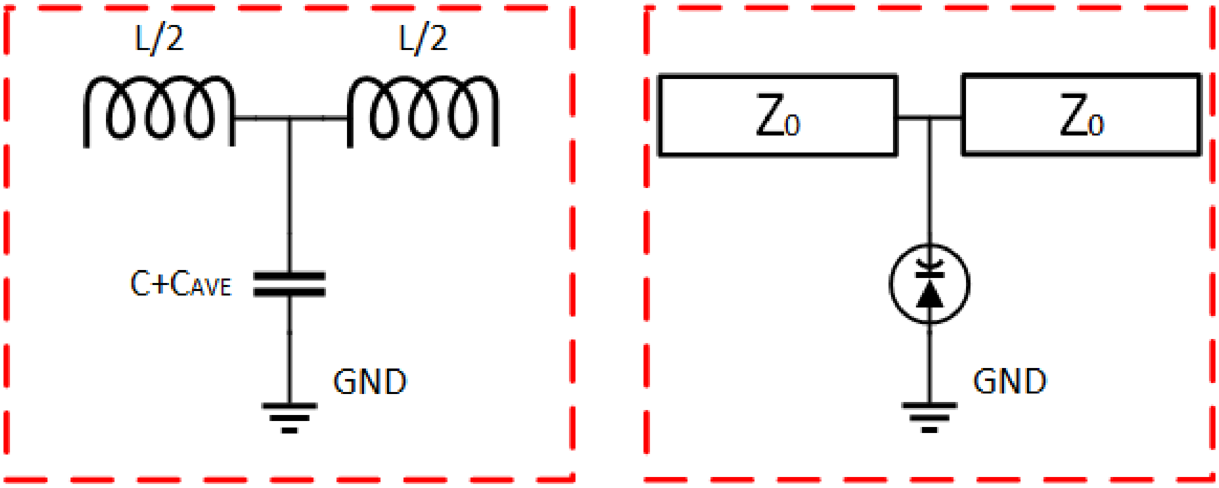

a) b)

Figure 23. a) Equivalent LC model (lumped model) for the unit cell of a periodically loaded NLTL; b) Unit cell of a periodically loaded nonlinear transmission line (distributed model).

4.1 Nonlinearity and Dispersion

The nonlinearity of the NLTLs mathematically is described by the C-V characteristic of an abrupt junction diode (5) [40]. The formula (5) shows that with an increase in the absolute value of the voltage *V* the capacitance of the varactor drops, which implies the nonlinear relation of C and V. The plot that showcases the nonlinear behaviour is shown in Fig. 24.

$$C(V) = \frac{C_0}{\sqrt{1 + \frac{V}{V_j}}} \tag{5}$$

Where, C_0 is a capacitance of the diode at a zero bias, V_j is a diode built-in potential.

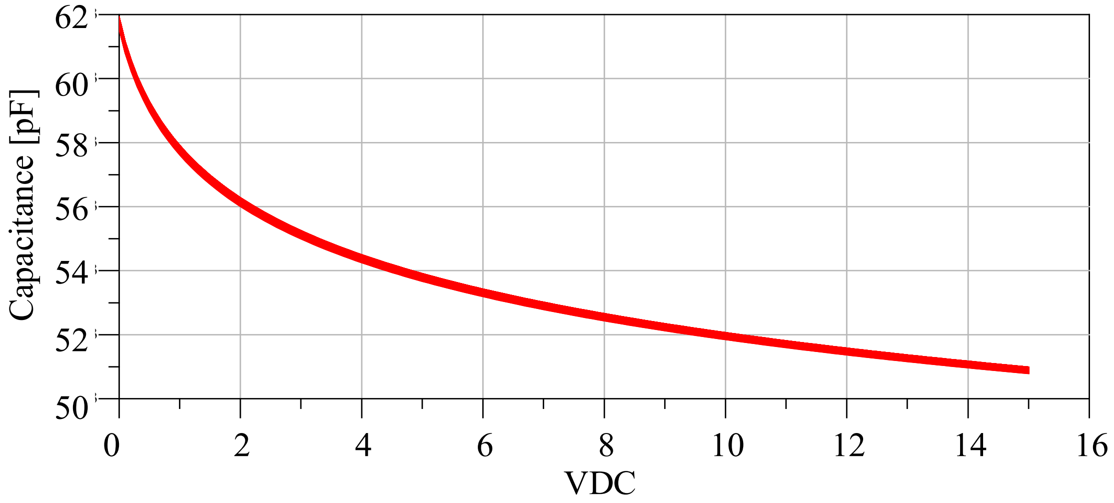

Figure 24. Plot of the C-V characteristic of an abrupt junction diode.

A general formula of a voltage-dependent phase velocity can be found using the formula (6). The voltage at the n*th* diode, the propagation delay and the total capacitance can be found as shown in (7), (8), (9), respectively [42].

$$v_p(V) = \frac{1}{\sqrt{L(C_l + C_d(V)}} \tag{6}$$

$$V_n(t) = V_{in}\big(t - nT(V)\big) \tag{7}$$

$$T(V) = T_V\sqrt{LC_T(V)} \tag{8}$$

$$C_T(V) = C_d(V) + C_l \tag{9}$$

The formula of the Bragg frequency is shown in (10) and (11). The Bragg frequency corresponds to a phase shift of 180° per stage [65].

$$\omega_{per} = \frac{2}{\sqrt{L(C_l + C_d(V))}} \tag{10}$$

$$f_{Bragg} = \frac{1}{\pi\sqrt{L(C_l + C_d(V))}} \tag{11}$$

The main characteristics of NLTL's behaviour depend on the ratio of the Bragg frequency to the frequency of the input pulse (12) [41] and the diode (small signal) cutoff frequency at bias voltage V (13).

$$f_{max,input} = \frac{1}{\pi t_{rise\ time}} \tag{12}$$

$$\omega_d = \frac{1}{C_d R_d} \tag{13}$$

Where, $t_{rise\ time}$ is the rise time of the input pulse, C_d is the diode capacitance, R_d is the parasitic series resistance.

Suppose the Bragg frequency is much higher than the frequency of the input pulse. In that case, the analysis of the NLTL can be done by using the equivalent LC model, which unit cell is shown in Fig. 23(a); otherwise, the approximation does not hold, and one needs to use the distributed model, which is shown in Fig. 23(b). Transmission lines with the characteristic impedance Z_0 and diodes represent the distributed model, where we need to consider the distributive characteristics such as the phase of the propagating signal.

While the ratio of the Bragg frequency and input frequency can determine whether one can apply the approximation, the ratio of the Bragg frequency to the cutoff of the diode can predict the output pulse waveform. If the Bragg frequency is much higher than the cutoff of the diode ($\omega_d \sim < \omega_{Bragg}$), then one deals with shock waves. On the other hand, if ($\omega_d > \omega_{Bragg}$), then one can see the propagation of solitons along the transmission line.

Dispersion is a variation in phase velocity with a frequency that has the opposite effect as nonlinearity, making the pulse wider and shorter in terms of amplitude [30]. To see how the dispersion affects the input pulse, one first must observe the ideal case with no dispersion. In other words, theoretically, the pulse should not be changed after propagation through a microstrip line—only one change one should see, which is a delay of the output pulse.

Using Advanced Design System (ADS), two simple microstrip lines (MLIN) were simulated with different lengths where the first MLIN is twice as long as the second one (Fig. 25).

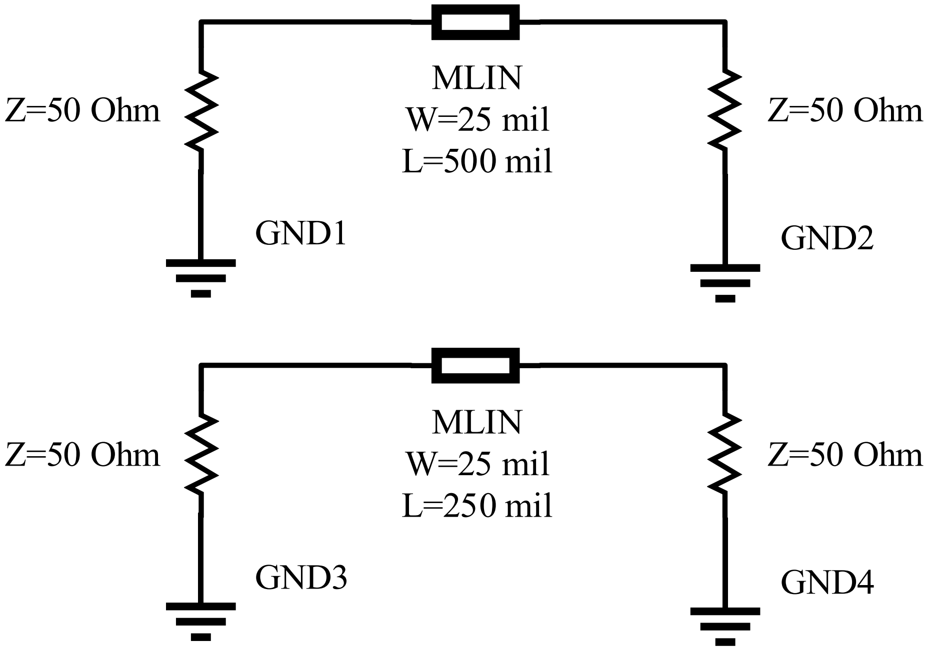

Fig. 25. Schematics of microstrip lines in ADS.

Afterward, the schematic was simulated, and a plot was created with a phase of S-parameters versus frequency. As shown in Fig. 26(a), there are linear trends for both MLINs, with the phase delay changing at the same rate as frequency. It is evident that zero-dispersion phase delay happens only because of different lengths of MLINs. However, in Fig. 26(b), if one introduces shunt varactor diodes, there is a deviation from the linear trend, leading to distortion of pulse shapes in output because of dispersion.

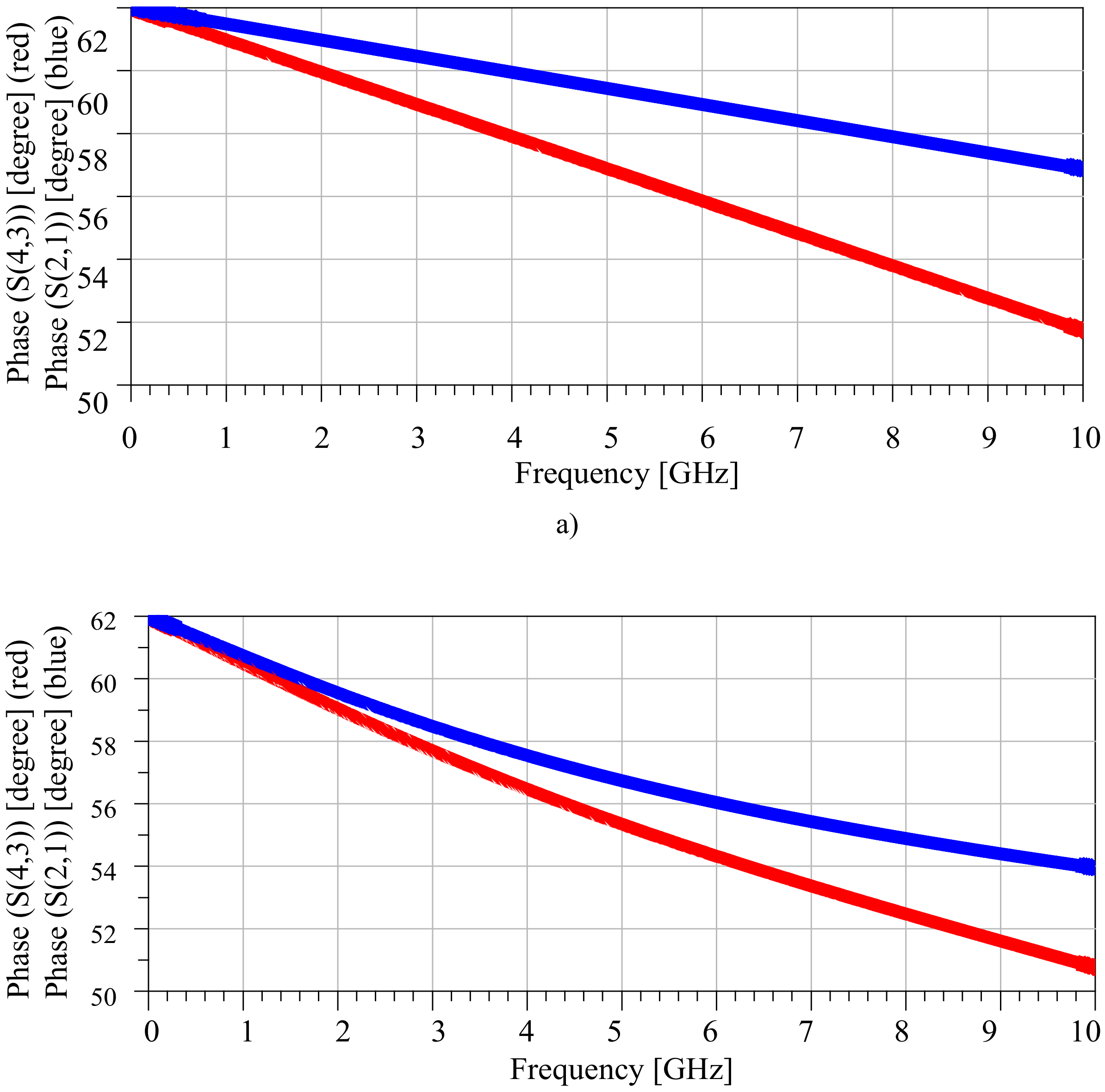

a)

b)

Fig. 26. Plot of phase versus frequency response simulated in ADS: a) linear trend; b) nonlinear trend due to dispersion.

First, before simulation, one needs to calculate a Bragg frequency (cutoff frequency) of our system. An input pulse of 5 V with 5 ns rise time, and an output pulse with a 200 ps rise time is needed. Also, an inductance of the transmission line is chosen to be 2 nH and capacitance to be 1 nF. The maximum operating frequency of the system can be calculated with Eq. (8) and a Bragg frequency with Eq. (7).

So, $f_{max} = \frac{1}{\pi \times 200\, ps} = 1.6\, GHz$ and $f_{Bragg} = \frac{1}{\pi\sqrt{2\times10^{-9}\times(0.58\times10^{-12}+1\times10^{-12})}} = 5.6\, GHz.$

Using the formula (1) or Fig. 24, the C-V characteristic of the diode can be found, which equals C(V) = 0.58 pF.

As one can see, the maximum operating frequency of our system is much less than the Bragg frequency, so simulation of a simplified version can be done with inductors in series and capacitors in parallel as transmission lines.

To understand how NLTLs work, first, how the rising edge works will be described. If one looks at Fig. 27, there are two circles 1 and 2 in the bottom picture. The region inside circle 1 represents the time when the diode is *On*-stage. In other words, it means that the diode is open and works as a short circuit. It implies the diode creates the short circuit with the ground, which one can see that the signal equals zero because all signal goes to the ground. However, it lasts only until the pulse amplitude reaches a particular value when the diode switches from *On*-stage to *Off*-stage. Since the diode is connected with the negative pin first, it will switch off when the pulse is positive. Usually, for this diode, -0.7 V is enough to switch them off. Regarding region 2, when the diode switches to Off-stage one, it has an open circuit with the ground, and all signal goes to the transmission line and reaches the output, so one sees the output pulse.

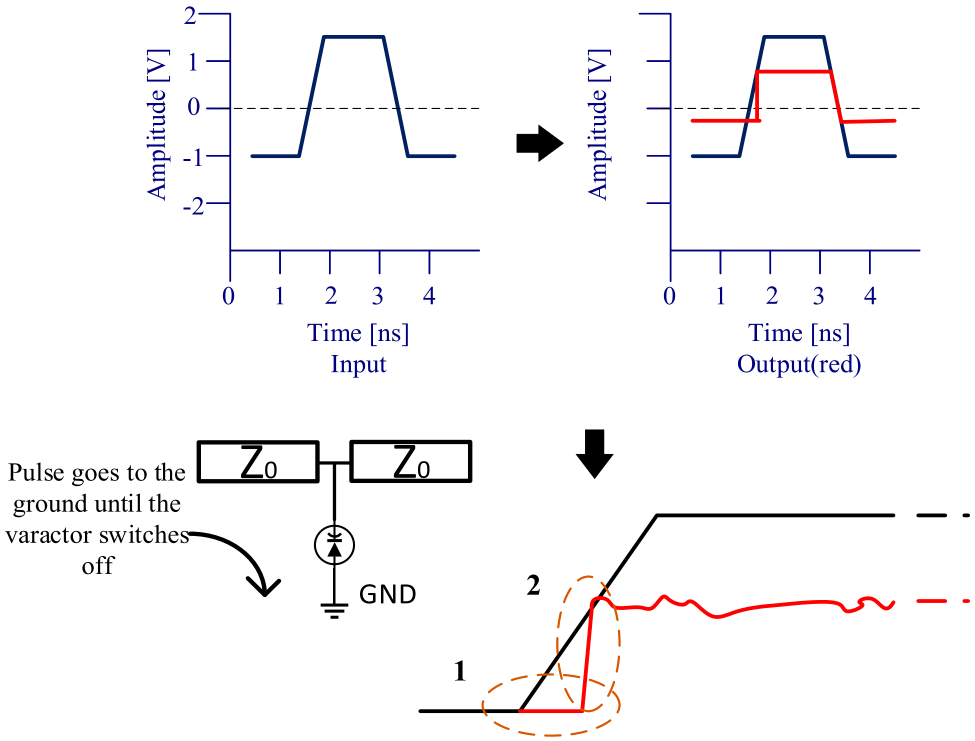

Pulse goes to the ground until the varactor switches off

Fig. 27. Diagram how the sharpening of the rising edge works.

When one changes the shunt diode’s polarity, switching the consequence of the On- and Off-stage of the diode happens. In Fig. 28, one can see exactly the opposite phenomenon happens. In fact, the diode works Off-stage initially; one can see the signal (the region 2) until it drops to approximately 0.7 V (region 1).

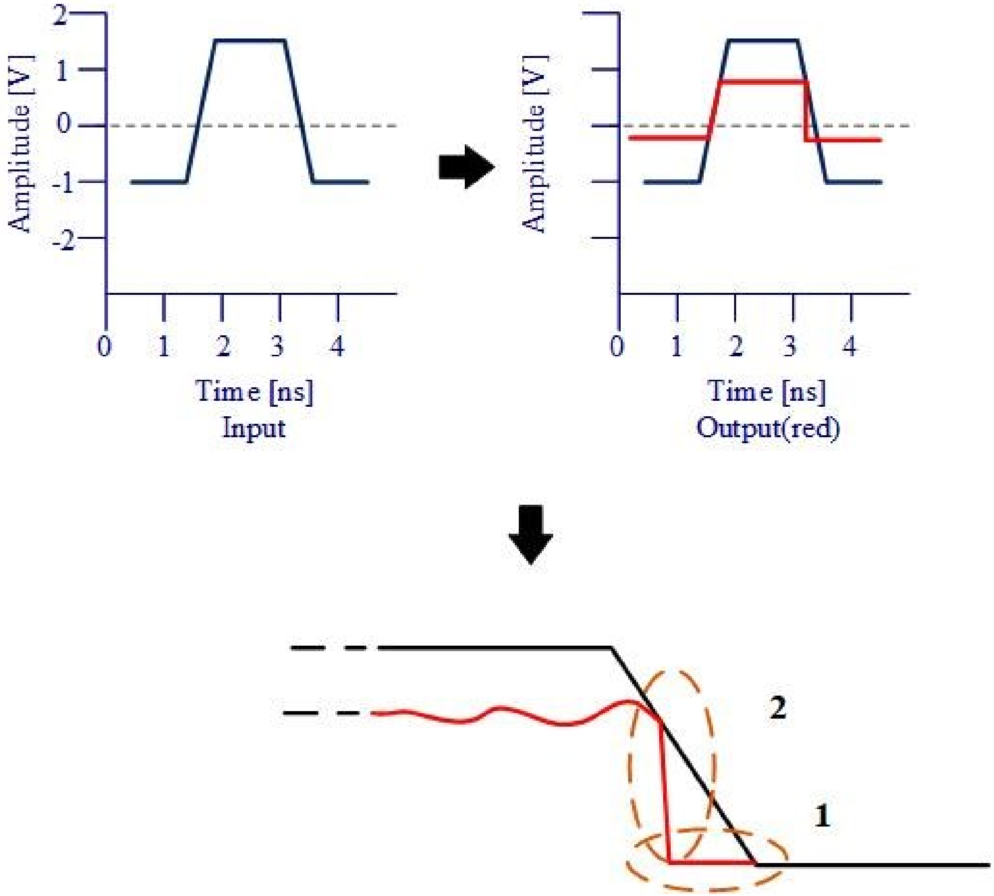

Fig. 28. Diagram how the sharpening of the falling edge works.

4.2 Design of the NLTL-based circuit

This work aims to design the Nonlinear Transmission Line (NLTL) based pulse sharpening system. The NLTLs are loaded periodically with reversed biased varactor diodes, which create the delay of the pulse propagation along the transmission line. It allows us to utilize this process to create ultra-fast Gaussian pulses in the range of a few tens of picoseconds. An analysis of the sharpening process is explicitly elaborated by implementing simulation in the Advanced Design System (ADS), which is used to calculate all graphs and diagrams presented in this section.

The schematic diagram can be found in Fig. 29, where section 1 is responsible for sharpening the rising edge while section 2 is responsible for sharpening the falling edge of the pulse. Section 1 consists of the transmission line connected with a varactor diode forward biased with a *DC* source. Still, it is reversed biased with the input pulse, and section 2 where the varactor diode should be forward biased to the input pulse.

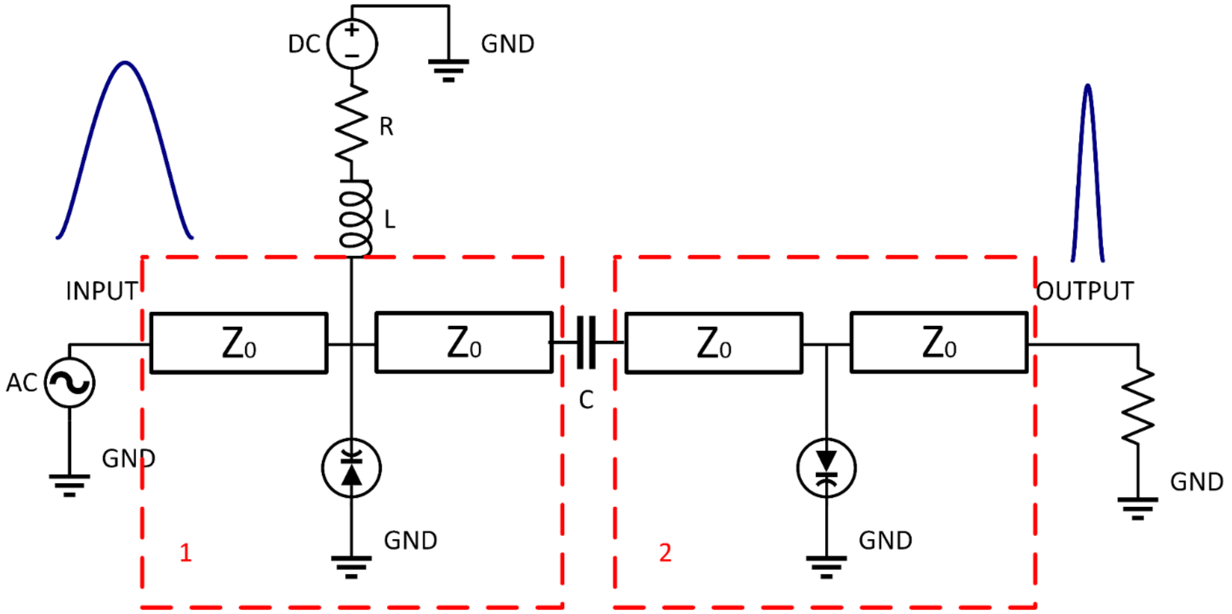

Figure 29. Sharpened output pulse after propagation along the NLTL

Initially, to test and see how the theoretical concept works in the simulations, the schematic of the cascaded unit cell is created in the Agilent ADS. As the input pulse for the NLTL, the ideal Gaussian pulse of 25 V with the pulse width of 250 ps and 180 ps rise time is chosen. Using (8), the highest frequency component of the input pulse is calculated to be approximately 1.7 GHz. In order to calculate the Bragg frequency and the diode cutoff frequency, one needs to know the simulation model of a varactor diode and the series inductance and the shunt capacitance of the transmission line. The varactor model is chosen to be MMSD4148T1G from Mouser Electronics. The diode has $C_0 = 0.619$ pF, $R_d = 1.138\ \Omega$ and $V_j = 0.4$ V. The series inductance of the transmission line of one unit is chosen to be 1 nH, and the shunt capacitance is to be 1 pF. The C-V characteristic of an abrupt junction diode according to (1) is then $C(V) = 77.6$ fF, the Bragg frequency according to (7) is then $f_{Bragg} = 12.3$ GHz. As one can see, the Bragg frequency is much higher than the frequency of the input signal. It means one can start analysis using a lamped model with an LC network. To predict if one can have solitons or shock waves, one needs to calculate the diode cutoff frequency. Using (9), it is found that $\omega_d = 11.3$ THz. The diode cutoff is much higher than the Bragg frequency. Thus, one has to work with solitons and an undesired ringing that comes with the solitons. However, solitons have a characteristic of having a gain in terms of amplitude, which means one can have a higher amplitude of the output pulse than the input pulse.

After many sessions of the simulations, it is found that by decreasing the inductance and capacitance of the transmission line by 10 % of the initial values, one can get an optimized output pulse. In Fig. 30, one can see the output pulse generated by 12 cascaded unit cells to sharpen the rise time and 5 unit cells cascaded to sharpen the falling edge.

From Fig. 30, one can see that amplitude increased from 25 V to 28.7 V, the rise time significantly decreased from 180 ps to 9 ps, as well as the fall time dropped to 24 ps, and the pulse width became 19 ps. Although there is a tremendous improvement in the pulse width, one has a ringing at the level of 4 V.

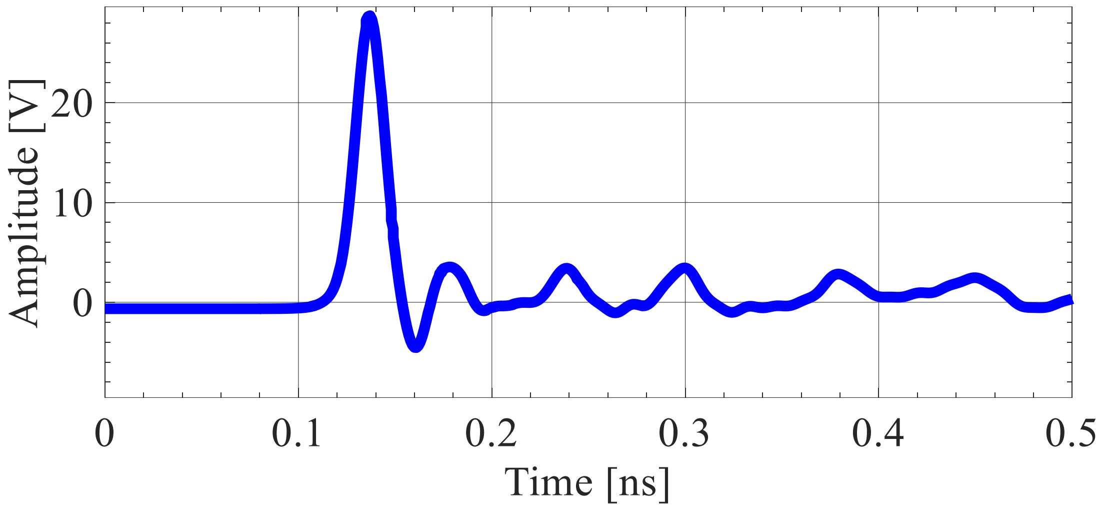

Figure 30. Plot of the output pulse of the lumped model of the NLTLs with the 25 V input pulse.

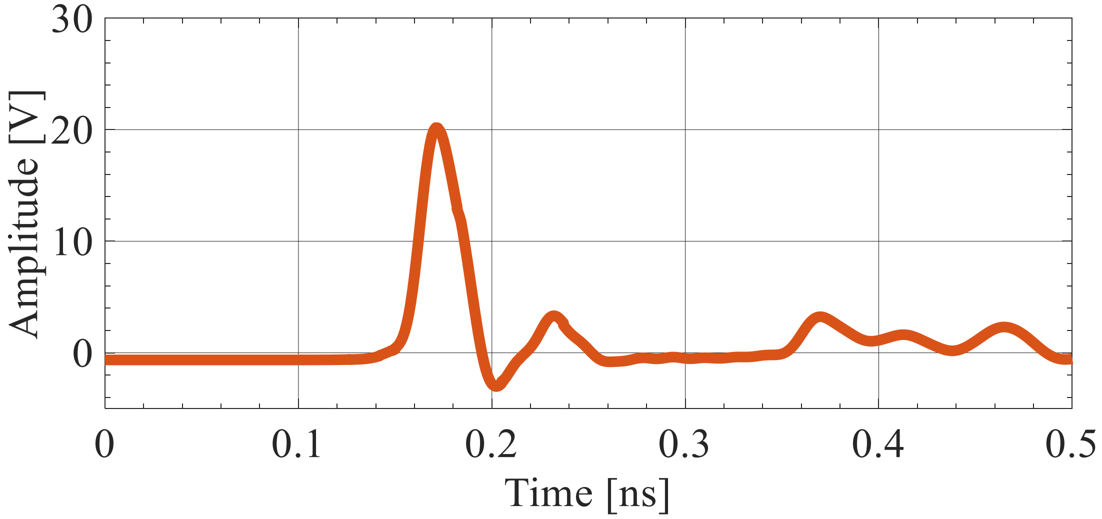

Figure 31. Plot of the output pulse of the lumped model of the NLTLs with the 17.5 V input pulse.

The next step is to use the Gaussian pulse produced by the actual physical circuit as the input for the NLTL. The waveform of this circuit is used to feed the NLTL. The input pulse amplitude is 17.5 V, and the pulse width is around 200 ps. In order to obtain a similar result as it is in Fig. 30, 14 unit cells for sharpening the rise time and 3 unit cells for sharpening the fall time are used. The output pulse can be observed in Fig. 31. It is apparent that one has a gain in amplitude (20 V) as well as a significant decrease in the rise time (9 ps), fall time (25 ps) and pulse width (24 ps).

The next stage is to use a distributed model of the NLTLs. The same analysis is done to generate the same result. To get a similar result, 11 unit cells are cascaded for the sharpening of the rise time, and only one unit cell is used to sharpen the fall time due to the noticeable drop in the amplitude when one tries to use more than one unit cell. The result can be seen in Fig. 32.

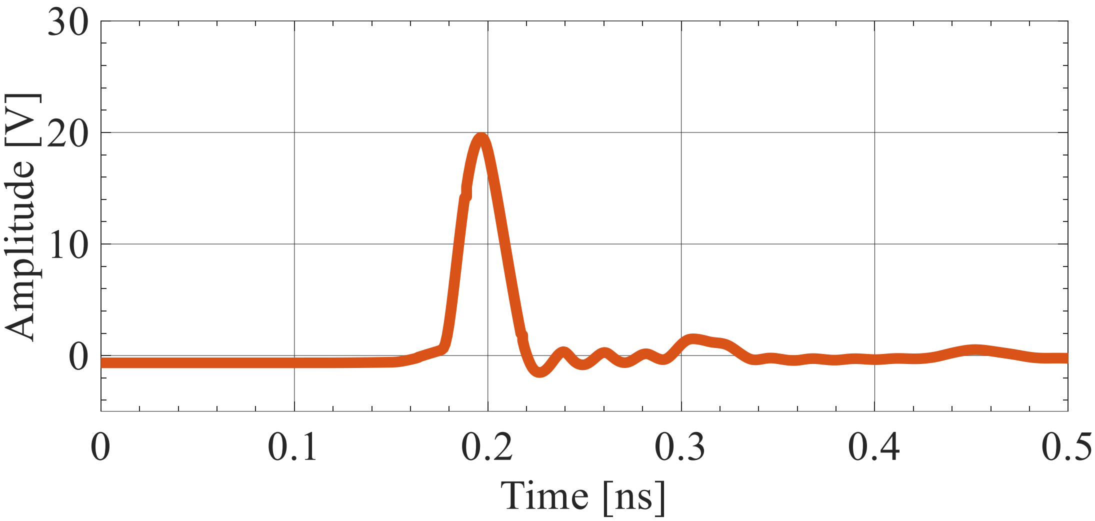

Figure 32. Plot of the output pulse of the distributed model of the NLTLs with the 17.5 V input pulse.

From Fig. 34, one can see an almost similar result with less ringing level and the rise time is 12 ps, fall time being 53 ps and the pulse width being 26 ps.

The reason to use around 12 unit cells to compress the rise time is that the rise time of the output pulse depends on the highest Bragg frequency of the last unit cell. It is found that the inductance and capacitance of the transmission line should be decreased from 1 nH and 0.1 pF for the first unit cell to 0.01 nH and 0.001 pF for the last unit cell, respectively. Hence, the Bragg frequency should be around 127 GHz. To obtain the rise time of 10 ps, the output pulse frequency (8) should be 31.83 GHz. It means that the Bragg frequency should be at least three times higher than the highest frequency component of the desired output pulse. Note that one can still have fewer unit cells to obtain a rise time of 10 ps by increasing the rate of a decrease of L and C from 10% to 30% or even 50%, but one will have a drop in the amplitude. Each succeeding unit cell cuts the previous unit cell's wave formation, resulting in an amplitude decrease.

The results obtained early are ideal and far from the realistic results. One should take into consideration that the diode model that was used for simulations is not able to represent the actual behaviour of the diodes fully. Since the length of the last stages is very short and comparable with the diodes' size, one should consider the pins of didoes as transmission lines as well.

Thus, the schematics should be updated with a shunt transmission line representing diodes' pins. In Fig. 33, one can see the modified schematic for the NLTLs.

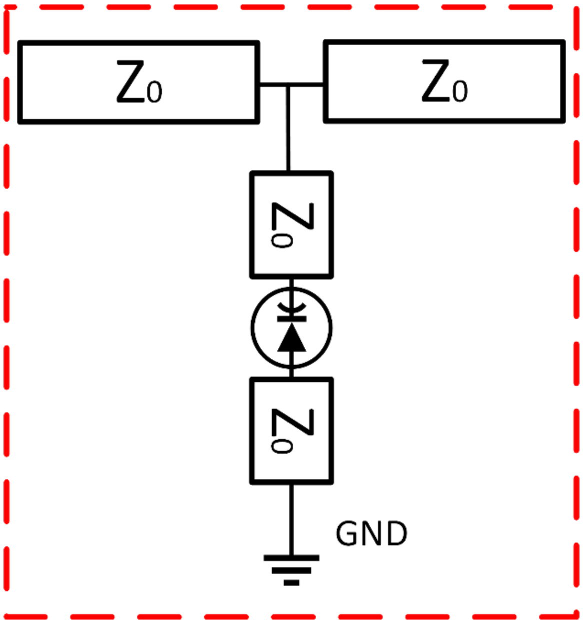

Figure 33. Modified unit cell with the pins of the diode taken into consideration.

It was found that if one increases the number of the unit cells and removes the last reverse polarity diode, one can mitigate the level of ringing. The trend of decrease in the length of transmission lines can be described by the formula of the exponential function shown below.

$$L_n = L_1(1-b)^{n-1} \tag{22}$$

Where, L_n is the length of the nth line and b = 0.15.

The simulation with a modified schematic was done by cascading twenty-one unit cells with the same polarity diodes. Moreover, a shunt inductor of 22 nH and a coupling capacitor were added at the end of the last unit cell, representing a high-pass filter to suppress the ringing further. The output pulse amplitude is 14.3 V, and the pulse width is 74 ps. The plot is shown in Fig. 34.

As one can see, with the introduction of parasitic elements in parallel with a transmission line, one gets worse results. In a parametric study, one found out that if one increases the capacitance of the diode model, one has the same undesired trend. Therefore, it can be claimed that shunt transmission lines represent shunt parasitic capacitors connected in parallel with diodes and make the output pulse worse. However, the results are more realistic and expected to be obtained in the experimental results.

In order to get even closer to the expected experimental result, one needs to proceed with the co-simulation with the layout structure. The co-simulation enables us to create physical parts (layouts) and add them to a circuit simulation to get closer to the experimental results. The result can be seen in Fig. 35.

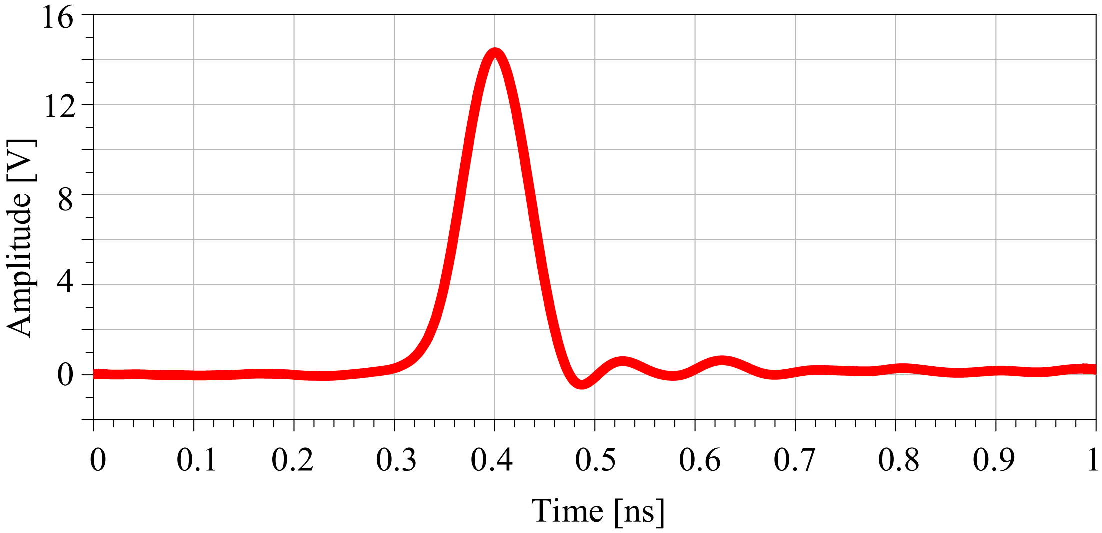

Figure 34. Plot of the output pulse of the distributed model of the NLTLs with the 17.5 V input pulse and modified unit cell.

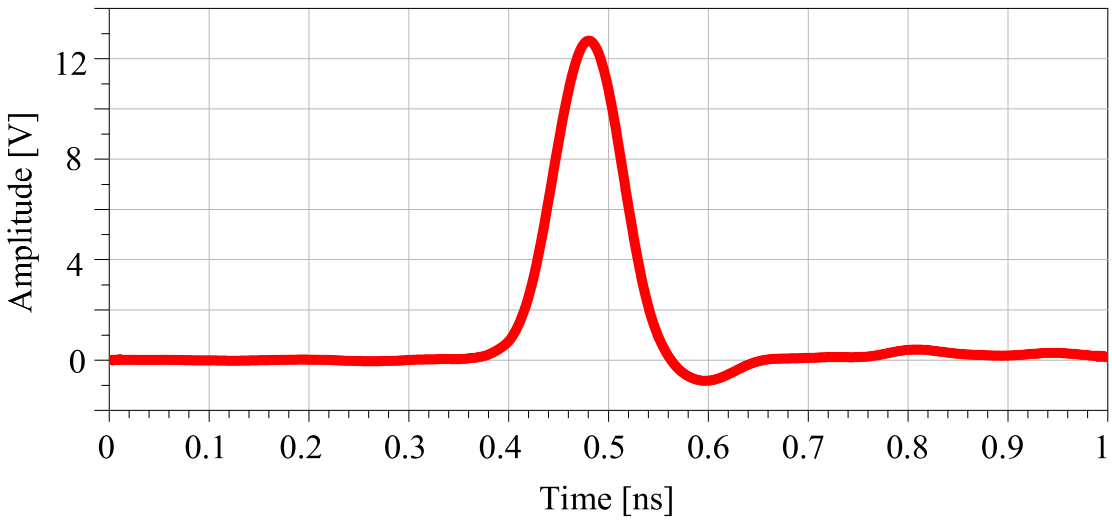

Figure 35. Plot of the co-simulation with layout structure.

It is evident from Fig. 35 that the result will be worse in terms of amplitude and the ringing level. The pulse width of the output pulse is 76 ps, and the amplitude is 12.8 V.

Furthermore, an optimization was done to improve the result obtained in Fig. 34 and Fig. 35. The next step is to have variable width the same as it was done with the length of the transmission lines. It was decided to implement the same exponential function with the width decreasing gradually from 44 mil to 10 mil. The output result can be seen in Fig. 36. In Fig. 36, the amplitude decreased by the parasitic effects from an additional transmission line is restored. The output pulse amplitude is 15.3 V, and the pulse width is 73 ps. Now is to proceed with the experimental testing.

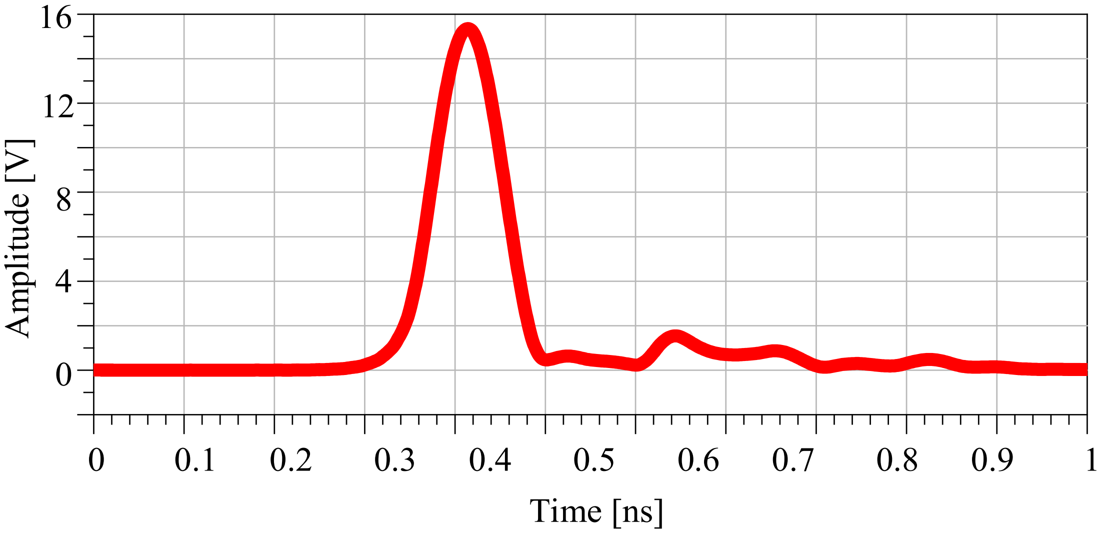

Figure 36. Output result of the modified length and width of the NLTL.

4.3 Experimental results

The experimental test is presented to validate the simulation results in this section. The system's configuration was chosen with all varactor diodes with the same polarity to sharpen the rising edge to show the process of the soliton and shock waves creation. One needs a very long transmission line to separate solitons, leading to significant losses. Thus, the circuit will be designed to utilize the shocks primarily with a partial soliton generation. Since the falling edge will not be sharpened enough and will have ringing, the high-pass filter will be used to suppress the ringing. The high-pass filter is a simple circuit with a capacitor in series and an inductor in parallel. The circuit consists of twenty-one unit cells, starting with a broader conductor and continuing with a narrower conductor in the end. Also, the length decreases gradually using the exponential decrease function mentioned before. It was done to minimize losses since the NLTL is a lossy network. The width of the NLTLs decreases slowly from 44 mil to 10 mil because 44 mil is a 50 Ohm transmission line, and 10 mil is the smallest distance one can fabricate in our laboratory. The circuit is shown in Fig. 37.

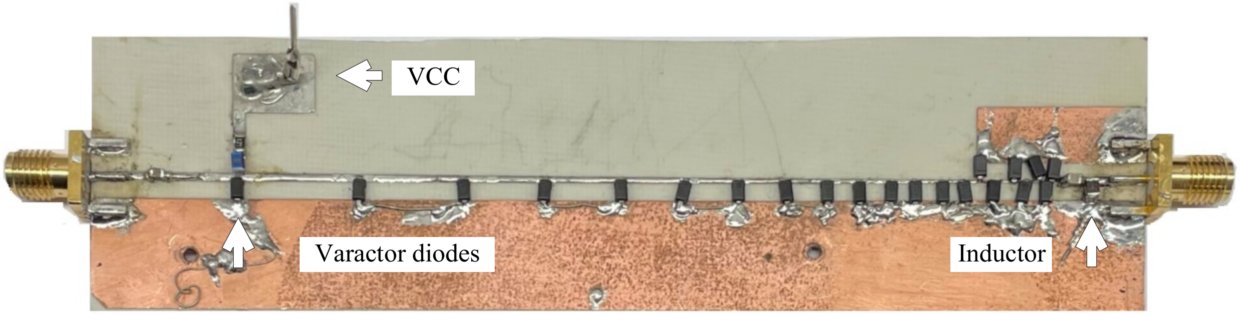

Figure 37. Fabricated circuit.

An input pulse of the circuit is a Gaussian pulse of 19 V with a pulse width of 500 ps. The output result is presented in Fig. 38. In Fig. 38, one can see that there are various outputs results.

Depending on the output inductor, one can tune the output pulse. An amplitude and a pulse width of the output pulse vary from 15.5 V to 12 V and from 220 ps to 175 ps, respectively.

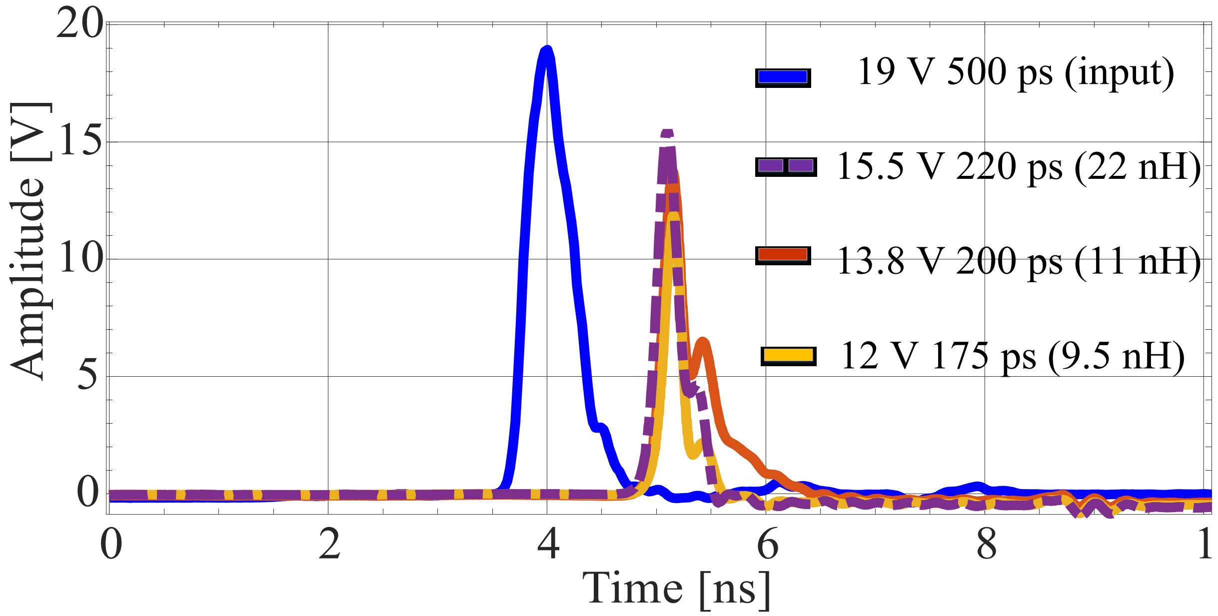

Figure. 38. Output results of the experimental results.

TABLE V
COMPARISON BETWEEN THE PERFORMANCES OF THE DIFFERENT NLTL-BASED SYSTEMS

Ref.	Pulse Shaping	Amplitude (V)	FWHM (ps)
[33]	NLTL-based	6.8	20
[41]	NLTL-based	3.95	95
[66]	NLTL-based	3.3	130
[67]	NLTL-based	1.0	70
[68]	NLTL-based	0.27	5
[69]	NLTL-based	2.97	129
This work	NLTL-based	12	175

As can be seen from Table V, previous published work could achieve shorter pulses at the cost of the output amplitude. My work aimed at generating a high signal output with a narrow pulse width of less than 200 ps and an amplitude as high as possible.

4.4 Conclusion

The NLTL-based circuits have a huge potential when it comes to sharpening both the rise time and fall time of any input pulse. Apart from sharpening the signal, they can obtain a gain of the amplitude if one can tune it properly. Two different analyses were established with the help of the lumped-element model and the distributed-element model. It was calculated mathematically and demonstrated by simulation the correlation among the fundamental characteristics of the NLTL, such as the Bragg frequency, the frequency of the output pulse, and the diode cutoff frequency. The design of the Ultra-fast Gaussian pulse generator that was presented in this thesis has reached the pulse width of 175 ps with an amplitude of output pulse of 12 V.

The output pulse of the presented design can be used in a vast range of applications. The range of applications can vary from sensing to imaging, such as characterization of buried objects in-ground, pavement damages detection, localization, and imaging of objects.

Chapter V

Conclusion and Future work

This thesis presented two different UWB radars that can be used for various imaging applications. The first configuration consists of the avalanche transistor-based circuit, SRD-based, and monopulse generating network. The second configuration is based on the NLTLs, a pulse shaping network. Both circuits are thoroughly studied, fabricated and tested for various applications, providing a deep analysis of pulse generation.

The main achievements associated with this work are related to ease and low-cost in-house fabrication design of the high-power Gaussian transmitter. The new, improved configuration of the SRD-based circuit was presented in this work. The separated biasing was implemented for the shunt and series SRDs which allowed us to achieve more control over the diodes' fast recovery transition time and therefore obtain a high power output pulse. Moreover, a smart technique for creating the monopulse was presented. Instead of using a differentiator for creating the monopulse, the pulse shifting technique was implemented, allowing us to eliminate the power loss associated with the poor performance of the differentiators.

Furthermore, the NLTL-based configuration was introduced to compare and analyze available ways of the narrow pulse generation used for imaging applications. The NLTL-based design has advantages, such as a simple configuration and a low voltage biasing (1V), and potentially can produce a pulse in the range of 10 ps. However, compared to the SRD-based circuit, the NLTL configuration could not provide a higher amplitude (13.8 V, 200 ps), while the SRD-based one could generate a 36 V, 200 ps pulse. The reason behind the low amplitude of the NLTL-based circuit is a lack of proper soliton creation. The solitons are reinforced pulses with higher amplitude than the input pulse. However, in order to generate solitons, one needs a significant number of the stage, around 100 stages and very precise soldering, which can be achieved only with the help of the industrial PCB equipment.

In future work, both types of configurations need improvement to be a finalized product. Although the SRD-based circuit produces a high-power pulse, its power consumption is significant. The first stage is the avalanche-based circuit which works in avalanche regions and needs a substantial biasing voltage. It can be improved further by replacing the avalanche transistor with a standard transistor and using a booster circuit to amplify the output pulse. Finally, the system can be powered with batteries and placed in a case to be portable and used in outdoor conditions.

Regarding the NLTL-based circuit, improvements can be made by increasing the stages' number. The increased number of stages can increase the cost and size of the final product. Thus, smaller varactors and precise machinery soldering might improve the circuit performance.

References

[1] S. and T. Sector, “RSS-220 - devices using Ultra-Wideband (UWB) technology,” Spectrum management and telecommunications, 31-Jul-2018. [Online]. Available: https://www.ic.gc.ca/eic/site/smt-gst.nsf/eng/sf09347.html. [Accessed: 23-May-2022].

[2] M. Skolnik, Radar Handbook, Third Edition. McGraw-Hill Education, 2008.

[3] S. O. Piper, "Homodyne FMCW radar range resolution effects with sinusoidal nonlinearities in the frequency sweep," Proceedings International Radar Conference, 1995, pp. 563-567, doi: 10.1109/RADAR.1995.522609.

[4] A. Karimov, R. Feghhi, F. M. Sabzevari, R. S. C. Winter, R. Fedosejevs and K. Rambabu, "Design and Development of a High-Power Pulse Transmitter for Underground Environmental Perception," in IEEE Transactions on Microwave Theory and Techniques, vol. 70, no. 5, pp. 2891-2903, May 2022, doi: 10.1109/TMTT.2022.3158322.

[5] L. Li, A. E.-C. Tan, K. Jhamb, and K. Rambabu, “Buried object characterization using ultra-wideband ground penetrating radar,” *IEEE Trans. on Microw. Theory Techn.*, vol. 60, pp. 2654-2664, 2012.

[6] A. Benedetto, F. Benedetto, M. R. D. Blasiis, and G. Giunta, “Reliability of signal processing technique for pavement damages detection and classification using ground penetrating radar,” *IEEE Sensors J.*, vol. 5, pp. 471-480, 2005.

[7] J. S. Lee, C. Nguyen, and T. Scullion, “A novel, compact, low-cost, impulse ground-penetrating radar for nondestructive evaluation of pavements,” *IEEE Trans. Instrum. Meas.,* vol. 53, pp. 1502-1509, 2004.

[8] O. Hirsch, M. Janson, W. Wiesbeck, and R. S. Thoma, “Indirect localization and imaging of objects in an UWB sensor network,” *IEEE Trans. Instrum. Meas*., vol. 59, pp. 2949-2957, 2010.

[9] Sabzevari, F.M., Winter, R.S., Oloumi, D. and Rambabu, K., 2020. A Microwave Sensing and Imaging Method for Multiphase Flow Metering of Crude Oil Pipes IEEE J. Sel. Topics Appl. Earth Observ. Remote Sens., 13, pp.1286-1297.

[10] Lee, Y., Park, J.Y., Choi, Y.W., Park, H.K., Cho, S.H., Cho, S.H. and Lim, Y.H., 2018. A novel non-contact heart rate monitor using impulse-radio ultra-wideband (IR-UWB) radar technology. Scientific reports, 8(1), pp.1-10.

[11] Kocur, D., Fortes, J. and Švecová, M., 2017. Multiple moving person tracking by UWB sensors: the effect of mutual shielding persons and methods reducing its impacts. EURASIP Journal on Wireless Commun. Network., 2017(1), pp.1-15.

[12] Oloumi, D., Winter, R.S., Kordzadeh, A., Boulanger, P. and Rambabu, K., 2019. Microwave imaging of breast tumor using time-domain UWB circular-SAR technique. *IEEE Trans. Med. Imag.*, 39(4), pp.934-943.

[13] S. M. Moghadasi and M. Dehmollaian, “Buried-Object Time-Reversal Imaging Using UWB Near-Ground Scattered Fields,” in *IEEE Trans. Geosci. Remote Sens.,* vol. 52, no. 11, pp. 7317-7326, Nov. 2014, doi: 10.1109/TGRS.2014.2311131.

[14] D. Oloumi, J.-W. Ting, and K. Rambabu, “Design of pulse characteristics for near-field UWB-SAR imaging,” *IEEE Trans. Microw. Theory Techn*., Vol. 64, pp. 2684-2693, 2016.

[15] J. Han and C. Nguyen, “On the development of a compact sub-nanosecond tunable monocycle pulse transmitter for UWB applications,” *IEEE Trans. Microw. Theory Techn.,* vol. 54, pp. 285-293, 2006.

[16] D. Oloumi, M. I. Pettersson, P. Mousavi, and K. Rambabu, “Imaging of oil-well perforations using UWB synthetic aperture radar”, *IEEE Trans. Geosci. Remote Sens.,* Vol. 53, No.8, Aug 2015, pp. 4510-4519.

[17] D. Oloumi and K. Rambabu, “Metal-Cased Oil Well Inspection Using Near-Field UWB Radar Imaging,” *IEEE Trans. Geosci Remote Sens.*, vol. 56, no. 10, pp. 5884-5892, 2018.

[18] D. Oloumi, P. Boulanger, A. Kordzadeh, and K. Rambabu, “Breast tumor detection using UWB circular-SAR tomographic microwave imaging,” in *2015 37th Annual International Conference of the IEEE Engineering in Medicine and Biology Society (EMBC),* 2015: IEEE, pp. 7063-7066.

[19] E. C. Fear, J. Bourqui, C. Curtis, D. Mew, B. Docktor, and C. Romano, “Microwave breast imaging with a monostatic radar-based system: A study of application to patients,” *IEEE Trans. Microw. Theory Techn.*, vol. 61, pp. 2119-2128, 2013.

[20] D. W. Winters, J. D. Shea, E. L. Madsen, G. R. Frank, B. D. V. Veen, and S. C. Hagness, “Estimating the breast surface using UWB microwave monostatic backscatter measurements,” *IEEE Trans. Biomed. Eng.*, vol. 55, pp. 247-256, 2008.

[21] J. R. Andrews, “Picosecond pulse generation techniques and pulser capabilities,” Applicat. Note AN-19, 2008.

[22] A. Matiss, A. Poloczek, A. Stohr, W. Brockerhoff, W. Prost, and F.-J. Tegude, "Sub-nanosecond pulse generation using resonant tunneling diodes for impulse radio," in Ultra-Wideband. ICUWB 2007. IEEE Int. Conf., 2007, pp. 354-359.

[23] D. Li and X. Yang, “Parameters analysis of Gaussian pulse circuit based on avalanche transistors,” in Microwave, Antenna, Propagation, and EMC Technologies, 2015 IEEE 6th Int. Symp., pp. 764-768.

[24] Y.-L. Guo, N.-N. Yan, S.-H. Guo, and G. Zeng, “500 ps/1 kV pulse generator based on avalanche transistor marx circuit,” in Microwave and Millimeter Wave Circuits and System Technology , 2013, © Int. Workshop, pp. 296-299.

[25] Z. Huang, Q. Fu, P. Chen, H. Yang, and X. Yang, “High power pulse generator based on avalanche transistor Marx circuit,” in Communication Problem-Solving, 2014 © IEEE Int. Conf., pp. 315-317.

[26] N. Beev, J. Keller, and T. E. Mehlstäubler, "Note: An avalanche transistor-based nanosecond pulse generator with 25 MHz repetition rate," Review of Scientific Instruments, vol. 88, p. 126105, 2017.

[27] D. Salameh and D. Linton, “Novel wide bandwidth GaAS sampling MMIC using microstrip based nonlinear transmission line (NLTL) and NLTL shock wave generator design,” in Microwave Conf., 1998. 28th European Conf., pp. 18-23.

[28] J. M. Johnson, J. M. Parson, D. V. Reale, A. A. Neuber, J. J. Mankowski, and J. C. Dickens, “10 kV, 44 ns pulse generator for 1 kHz trigatron reprate operation of NLTL,” in Power Modulator and High Voltage, 2014 IEEE Int. Conf, 2014, pp. 108-110.

[29] Y. Ma and E. C. Kan, “Accurate indoor ranging by broadband harmonic generation in passive NLTL backscatter tags,” *IEEE Trans. Microw. Theory Techn.,* Vol. 62, pp. 1249-1261, 2014.

[30] Ryogo Hirota and Kimio Suzuki, “Theoretical and Experimental Studies of Lattice Solitons in Nonlinear Lumped Networks,” Proceedings of the IEEE, vol. 61, no. 10, pp. 1483{1491, October 1973.

[31] Mark J. W. Rodwell, Masayuki Kamegawa, Ruai Yu, Michael Case, Eric Carman, and Kirk S. Giboney, “GaAs Nonlinear Transmission Lines for Picosecond Pulse Generation

and Millimeter-Wave Sampling," IEEE Transactions on Microwave Theory and Techniques vol. 39, no. 7, july 1991.

[32] Mark J. W. Rodwell, "Picosecond Electrical Wavefront Generation and Picosecond Optoelectronic Instrumentation," Ph.D. dissertation, Dept. Elect. Eng., Stanford Univ., Stanford, CA, 1987.

[33] Mark J. W. Rodwell, Scott T. Allen, Ruai Y. Yu, Michael G. Case, Uddalak Bhattacharya, Madhukar Reddy, Eric Carman, Masayuki Kamegawa, Yoshiyuki Konishi, Joe Pusl, and Rajasekhar Pullela, "Active and Nonlinear Wave Propagation Devices in Ultrafast Electronics and Optoelectronics," Proceedings of the IEEE, vol. 82. no. 7, July 1994.

[34] M. Remoissenet, "Waves Called Solitons, Concepts and Experiments," New York: Springer-Verlag, 1999, ch. 1.

[35] D. Salameh and D. Linton, "Study of the Effect of Various Parameters on Nonlinear Transmission-Line (NLTL) Performance," IEEE Transactions on Microwave Theory and Techniques, vol. 47, no. 3, march 1999.

[36] D. Salameh and D. Linton, "Microstrip GaAs Nonlinear Transmission-Line (NLTL) Harmonic and Pulse Generators," IEEE Transactions on Microwave Theory and Techniques, vol. 47, no. 7, july 1999.

[37] M. Adnan and E. Afshari, "Efficient Microwave and Millimeter-Wave Frequency Multipliers Using Nonlinear Transmission Lines in CMOS Technology," IEEE Transactions on Microwave Theory and Techniques, vol. 63, no. 9, September 2015.

[38] Hui Shi, W.-M. Zhang, C. W. Domier, N. C. Luhmann, Jr., L. B. Sjogren, and H.-X. L. Liu, "Novel Concepts for Improved Nonlinear Transmission Line Performance," IEEE Transactions on Microwave Theory and Techniques, vol. 43, no. 4, April 1995.

[39] D. Salameh and D. Linton, “Nonlinear Transmission Line (NLTL) Design as a Pulse Generator,” IEEE MTT/ED/AP/LEO Societies Joint Chapter, 2nd High Frequency Postgraduate Student Colloquium, United Kingdom and Republic of Ireland Section, 1996.

[40] Fan Yu, Keith G. Lyon, and Edwin C. Kan, “A Low-Power UWB-IR Transmitter by Tapered Nonlinear Transmission Lines,” IEEE Microwave and Wireless Components Letters, vol. 22, no. 12, December 2012.

[41] MuhibUr Rahman and Ke Wu, “A Nonlinear Transmission Approach to Compressing Rise and Fall Time in Picosecond Pulse Generation,” IEEE Transactions on Instrumentation and Measurement, vol. 70, 2021.

[42] Mark Kintis, Xing Lan, Flavia Fong, Donald Sawdai, Kwok Loi, Keith Kono, and Augusto Gutierrez, “An MMIC Pulse Generator Using Dual Nonlinear Transmission Lines,” IEEE Microwave and Wireless Components Letters, vol. 17, no. 6, June 2007.

[43] O. Ozgur Yildirim, David S. Ricketts, and Donhee Ham, “Reflection Soliton Oscillator,” IEEE Transactions on Microwave Theory and Techniques, vol. 57, no. 10, October 2009.

[44] Mohammad Samizadeh Nikoo and Seyed Morad-Ali Hashemi, “Analysis of the Power Transfer to a Nonlinear Transmission Line,” IEEE Transactions on Microwave Theory and Techniques, vol. 65, No. 11, November 2017.

[45] Kasra Payandehjoo, “Study of Nonlinear Transmission Lines and their Applications,” MEng. thesis, Dept. Elect. Eng., McGill University Montreal, Canada, October 2006.

[46] Miles M. Turner, Greg Branch, and Paul W. Smith, “Methods of Theoretical Analysis and Computer Modeling of the Shaping of Electrical Pulses by Nonlinear Transmission Lines and Lumped-Element Delay Lines,” IEEE Transactions on Electron Devices, vol. 38, no. 4. April 1991.

[47] David S. Ricketts and Donhee Ham, “Electrical Solitons Theory, Design, and Applications,” New York: CRC Press, 2010, ch. 7.

[48] Michael Garth Case, “Nonlinear Transmission Lines for Picosecond Pulse, Impulse and Millimeter-Wave Harmonic Generation,” Ph.D. dissertation, Dept. Elect. Eng., University of California, Santa Barbara, 1993.

[49] Xudong Wang and R. Jennifer Hwu, “Theoretical Analysis and FDTD Simulation of GaAs Nonlinear Transmission Lines,” IEEE Transactions on Microwave Theory and Techniques, vol. 47, no. 7, July 1999.

[50] L. Zou, S. Gupta, and C. Caloz, “A simple picosecond pulse generator based on a pair of step recovery diodes,” *IEEE Trans. Microw. Wireless Compon. Lett.,* Vol. 27, pp. 467-469, 2017.

[51] J. Han and C. Nguyen, “Coupled-slotline-hybrid sampling mixer integrated with step-recovery-diode pulse generator for UWB applications,” *IEEE Trans. Microw. Theory Techn.*, Vol. 53, pp. 1875-1882, 2005.

[52] J. Han and C. Nguyen, “A new ultra-wideband, ultra-short monocycle pulse generator with reduced ringing,” *IEEE Trans. Microw. Wireless Compon. Lett.*, Vol. 12, pp. 206-208, 2002.

[53] J. Han and C. Nguyen, “Ultra-wideband electronically tunable pulse generators,” *IEEE Trans. Microw. Wireless Compon. Lett.*, Vol. 14, pp. 112-114, 2004.

[54] T. Xia, A. S. Venkatachalam, and D. Huston, “A high-performance low-ringing ultrawideband monocycle pulse generator,” *IEEE Trans. Instrum. Meas.*, Vol. 61, pp. 261-266, 2012.

[55] J. S. Lee, C. Nguyen, and T. Scullion, “New uniplanar subnanosecond monocycle pulse generator and transformer for time-domain microwave applications,” *IEEE Trans. Microw. Theory Techn.,* Vol. 49, pp. 1126-1129, 2001.

[56] R. Feghhi, D. Oloumi, and K. Rambabu, “Design and Development of an Inexpensive Sub-Nanosecond Gaussian Pulse Transmitter,” *IEEE Trans. Microw. Theory Techn.,* pp. PP. 1-10, 2019.

[57] R. Feghhi, D. Oloumi, and K. Rambabu, “Tunable Subnanosecond Gaussian Pulse Radar Transmitter: Theory and Analysis,” *IEEE Trans. Microw. Theory Techn*, Vol. 68, 2020.

[58] B. Biswas, R. Ghatak, and D. R. Poddar, “A Fern Fractal Leaf Inspired Wideband Antipodal Vivaldi Antenna for Microwave Imaging System,” *IEEE Trans. Antennas Propag.,* Vol. 65, pp. 6126-6129, No. 11, November 2017.

[59] AH Ameri, “Long-Range Ultra-Wideband Radar Sensor for Industrial Applications,” Chapter 5. pp. 36-67, 2012.

[60] Stephen A. Maas, “Nonlinear Microwave and RF Circuits”, 2nd ed, London, Boston, Artech House, 2003, pp 71-73.

[61] J.L. Moll, S. Krakauer, and R. Shen, "P-N Junction Charge-Storage Diodes," *Proc. IRE*, Vol. 50, no. 1, pp. 43-53, 1962.

[62] J.L. Moll, S.A. Hamilton, “Physical Modeling of the Step Recovery Diode for Pulse and Harmonic Generation Circuits,” *Proc. the IEEE*, Vol. 57, no. 7, pp. 1250-1258, 1969

[63] J. Ceremuga, “A dynamic model of the p-n-n$^+$ Step Recovery Diodes for the numerical analysis of pulse circuits,” Solid-State Electronics Vol. 24, pp. 501-510, 1981

[64] AH Ameri, G. Kompa, A. Bangert, “Balanced Pulse Generator for UWB Radar Application” Proc. of the 8th European Radar Conf., pp. 198-201, 2011.

[65] K. G. Lyon and E. C. Kan, “Microwave pulse generation using the Bragg cutoff of a nonlinear transmission line,” 2008 IEEE MTT-S International Microwave Symposium Digest, 2008, pp. 1461-1464.

[66] J. Zhou, Q. Lu, F. Liu, and Y. Li, “A novel picosecond pulse generation circuit based on SRD and NLTL,” PloS One, vol. 11, no. 2, Aug. 2016, Art. no. e0149645.

[67] E. Afshari and A. Hajimiri, "Nonlinear transmission lines for pulse shaping in silicon," in IEEE Journal of Solid-State Circuits, vol. 40, no. 3, pp. 744-752, March 2005, doi: 10.1109/JSSC.2005.843639.

[68] Y. Konishi, M. Kamegawa, M. Case, Ruai Yu, S. T. Allen and M. J. W. Rodwell, "A broadband free-space millimeter-wave vector transmission measurement system," in IEEE Transactions on Microwave Theory and Techniques, vol. 42, no. 7, pp. 1131-1139, July 1994, doi: 10.1109/22.299747.

[69] M. Ponton, F. Ramirez, A. Suarez and J. P. Pascual, "Applications of Pulsed-Waveform Oscillators in Different Operation Regimes," in IEEE Transactions on Microwave Theory and Techniques, vol. 57, no. 12, pp. 3362-3372, Dec. 2009, doi: 10.1109/TMTT.2009.2034068.